INVESTIGATION OF PHONON TRANSPORT AND THERMAL BOUNDARY CONDUCTANCE AT THE INTERFACE OF FUNCTIONALIZED SWCNT AND POLY (ETHER-KETONE)

A Thesis
Presented to
The Academic Faculty

by

Haoxiang Huang

In Partial Fulfillment
of the requirements for the Degree
Master of Science in the
School of Mechanical Engineering

Georgia Institute of Technology
August 2016

INVESTIGATION OF PHONON TRANSPORT AND THERMAL BOUNDARY CONDUCTANCE AT THE INTERFACE OF FUNCTIONALIZED SWCNT AND POLY (ETHER-KETONE)

Approved by:

Dr. Satish Kumar, Advisor
School of Mechanical Engineering
Georgia Institute of Technology

Dr. Satish Kumar
School of Material Science & Engineering
Georgia Institute of Technology

Dr. Zhuomin Zhang
School of Mechanical Engineering
Georgia Institute of Technology

Date Approved: 07/05/16

ACKNOWLEDGEMENTS

I would first thank Dr. Satish Kumar from the department of Mechanical Engineering for his guidance to my research work. Next, I would thank Dr. Liang Chen who contributed his source codes and provided valuable research related suggestions. I appreciate help of Dr. Vikas Varshney from Air Force Research Lab, who provided suggestions for atomistic simulations even during his busy time. I would like to thank my co-workers Zhequan Yan, Jialuo Chen, Man Prakash Gupta, David Brown and my friend Yan Wang who encouraged me throughout my research work at Georgia Tech. Besides these people in my research group, I would thank my M.S. thesis committee member for valuable suggestions and other faculty members who instructed various courses I took; they taught me fundamentals of engineering and science. Finally, I would thank my parents who encourage me to pursue my own career and personal goal.

TABLE OF CONTENTS

LIST OF TABLES

Page

LIST OF FIGURES

NOMENCLATURE

Symbols

A	Cross-section Area
a	Lattice Constant
d	Direction of Angle in Dihedral and Improper Potential
E	Energy
G	Thermal Boundary Conductance
g	Energy Spectrum
J	Heat Flux
j	j^{th} atom in each unit cell for SED derivation
K	Stiffness of Bonding
k	Thermal Conductivity
k_B	Boltzmann Constant
l	Symbol of unit cell for SED derivation
m	Mass of Single Atom
N	Degrees of Freedom
N	Total Number of Unit Cells
n	Represents nth unit cell
N_{CNT}	Total Number of CNT Atoms
N_{sub}	Total Number of substrate Atoms
p	Total Atoms in Unit Cell

Q	Heat Rate
Q	Normal Mode Coordinate
q	Particle Charge
r	Distance
r_o	Equilibrium Distance
t	Time
T	Temperature
$\overline{T}$	Normal Mode Kinetic Energy
U	Vector Amplitude of Normal Mode
u	Displacement between Two Atoms
$\dot{u}$	Velocity of Atom in SED Derivation
v	Velocity of Atom
α	Dimensions
Δ	Difference
κ	Wave-vector
ω	Frequency
ϕ	Improper Torsion Angle
π	the Ratio of a Circle's Circumference to Diameter
ρ	Phonon Density of States
τ	Time Constant
θ	Spectral Energy Density
θ_o	Equilibrium Angle between Neighbor Atoms

σ	Distance Corresponding to Zero Inter-Particle Potential
ε	Depth of Potential Well of Lennard-Jones Potential
ε_o	Dielectric Constant

Subscripts

1	1st Frequency Band
2	2nd Frequency Band
3	3rd Frequency Band
4	4th Frequency Band
eq	Equilibrium State
neq	Non-equilibrium State
i	ith Atom in Force Field
j	jth Atom in Force Field
k	kth Atom in Force Field
l	lth Atom in Force Field
sub	substrate
tot	Total

Abbreviations

3-D	Three dimensional
ALD	Anharmonic Lattice Dynamics
BTE	Boltzmann Transport Equation
CNT	Carbon Nanotube

DFT	Density Functional Theory
GK	Green-Kubo
MD	Molecular Dynamics
NEMD	Non-equilibrium Molecular Dynamics
NMD	Normal Mode Decomposition
PEK	Poly (ether) Ketone
SED	Spectral Energy Density
SWCNT	Single-walled Carbon Nanotube
TBC	Thermal Boundary Conductance
VC	Virtual Crystal Approximation
vdW	van der Waals

CHAPTER 1

INTRODUCTION

Nanoscale thermal transport had attracted great attention in recent years, as it could solve potential problems in multiple areas such as medical treatment, electronic devices, industrial processing and renewable energy [1]. Polymer materials were broadly studied and applied in various engineering fields as very good electrical and thermal insulators, while researchers also realized that thermally conductive polymers could replace the metallic portions in many industrial applications, e.g., in power generators; for automotive, aerospace and electronic packaging applications [2].

For electronic systems, the composite materials used for electronic packaging were required to have a thermal conductivity greater than 100 W/m-K [3]. In general, polymers have low thermal conductivity (0.1-1.0 W/m-K) at room temperature. To improve the thermal properties of polymers, carbon based nanostructured materials were chosen as fillers due to their high electrical and thermal conductivities [2, 4]. Graphite, constituted of layers of graphene sheets, exhibited an intrinsic thermal conductivity of approximately 800 W/m-K or even higher; the thermal conductivity of graphene or carbon nanotubes (CNT) was in the range of ~2000-6000 W/m-K [2, 5, 6]. Since the filler loadings of the polymer would also change the mechanical properties of a polymer composite significantly, the weight of fillers and the processing techniques are very important. Even though metallic and ceramic fillers could enhance the thermal conductivity and electrical conductivity of a polymer matrix, the density, the size of fillers and the experimental treatment would limit the behavior of the thermal conductivity of the polymer composite [2, 7-9]. When CNTs were used as fillers, the thermal conductivity of corresponding polymeric nanocomposites increased effectively [10]. The heat transfer at the

interface of carbon-based fillers such as polymer-CNT interface is quite important as it can limit the enhancement in effective thermal conductivity of polymers. The interfacial thermal resistance of polymer-CNT was measured or computed to be order of 10^{-8} m^2K/W for some polymer materials [1, 11, 12], which can be enhanced by engineering the interfaces.

Poly (ether ketone) (PEK) is a promising polymer material whose electrical and thermal conductivities were expected to be improved by the insertion of carbon based fillers [13]. *Moon et al.* [13] indicated that for CNT weight ratio of 28% (28 wt. %), the thermal conductivity increased to 27 W/m-K at 390 K, which is about 100 times larger when no fillers are used and 10 times larger than that of 5 wt. % CNT, see Figure 1. When PEK was grafted with 20 wt. % CNTs, the electrical conductivity (~240 ± 88 S/m) of PEK-g-CNT fiber had been shown to rise by six orders of magnitude.

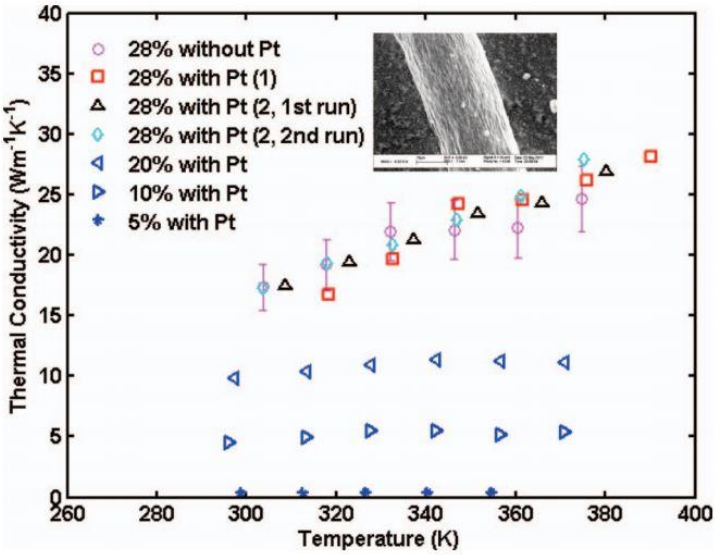

Figure 1: Thermal conductivity of FWCNTs with various percentages of grafted PEK. Adapted from Reference [2].

Table. 1 Mechanical properties & electrical conductivity of PEK and various PEK-g-FWNT Fillers. Adapted from Reference [13].

FWNT content (%)	Tensile Strength (MPa)	Tensile Modulus (GPa)	Electrical conductivity (S/m)
0	486 ± 12	10.6 ± 0.3	N/A
1	297 ± 7	6.6 ± 0.3	N/A
5	359 ± 11	9.4 ± 0.7	$2.1 \times 10^{-4} \pm 5.9 \times 10^{-6}$
10	191 ± 6	7.2 ± 0.5	25 ± 7
20	122 ± 11	17.3 ± 1.3	240 ± 88

Because of the exceptional increase in thermal conductivity of CNT/PEK nanocomposite, exploration of the interfacial thermal transport at the interface of CNT and PEK is of significant interest for scientists and engineers. In this thesis, atomistic computational methodologies are used to investigate the thermal transport, especially phonon interactions, at the interface of CNT and PEK. Using non-equilibrium molecular dynamics (NEMD) method, a (20, 20) armchair CNT, embedded in PEK matrix with different degrees of PEK grafting is used to analyze interfacial thermal transport. The interfacial thermal boundary conductance (TBC) at PEK/CNT interface is explored to get insights into remarkable increase in the thermal conductivity of PEK/CNT fibers. In order to understand the physics of thermal interactions, the phonon power spectra are computed for different numbers of crosslinks in different frequency regimes. Transient decay in spectral temperature of CNTs is studied, when subjected to a high temperature pulse, for different bonded cases to decipher the thermal coupling between CNT and PEK in different frequency bands. Brief descriptions of the content of different Chapters of thesis are provided next.

In Chapter 2, a critical assessment of the literature on the polymeric composite with carbon based fillers and polymer crosslinks for thermal transport is reported. In particular, there

will be a focus on simulations of interfacial thermal transport in polymeric composites with carbon based fillers. Especially, there will be discussions about the functionalization effect (crosslinks bonded on the surface of nanostructured materials fillers in surrounding matrix) on thermal transport. Even though some investigations already developed experimental or computational models to understand how fillers and functionalization were critical for changing the efficiency of thermal transport, the phonon interactions between atoms of fillers and polymer matrix were not well understood yet.

In Chapter 3, the computational model and theoretical basis used in this thesis are presented. Molecular dynamics (MD) simulation methodologies and the spectral energy density (SED) method is introduced for calculating the phonon properties of CNT for isolated and embedded cases. The non-equilibrium molecular dynamics method is introduced for computing interfacial thermal boundary conductance (TBC) for CNT embedded in PEK. To further understand the phonon interactions between CNT and PEK matrix, the equilibrium and transient phonon spectra of CNT and PEK atoms are computed for embedded CNT using the Fourier Transform of velocity profiles. Equilibrium spectra is used to visualize the spectra overlapping between CNT and PEK, which also provide guidance in dividing the spectrum in frequency bands and analyzing thermal transport in different bands. The calculations of spectral temperatures in different frequency bands deepen the elucidation of phonon transport at the interface of CNT and PEK. An algorithm is developed for cross-linking CNT with chains of PEK and a total of 6 different cases studied: 1 crosslink, 5 crosslinks, 10 crosslinks, 20 crosslinks, 40 crosslinks and 80 crosslinks CNT. The calculations for spectral temperatures and TBC will be reported for those cases.

In Chapter 4, first, the results for thermal boundary conductance (TBC) between PEK and CNT are presented to elucidate how the number of crosslinks bonded on CNT affects the efficiency of thermal transport. Next, phonon dispersion curves of isolated and embedded CNTs are estimated by SED is shown and interfacial energies transfers in different frequency bands are discussed. The frequency regime is divided into 4 bands based on the overlapping of spectra and the spectral temperature calculations of these frequency bands for both non-bonded and bonded cases (~ CNT cross-linked with PEK) are discussed to decipher which band is the most efficient for energy transfer and how it is affected by increasing the number of cross-links between CNT and PEK. To understand how the atoms in crosslinks participate in energy exchange, CNTs are heated using short temperature pulses and then relaxed, and the instant spectra at different time instants and relaxation time of different frequency bands are analyzed. Finally, Chapter 4 provides the discussion on the comparison with previous results in the literature.

Chapter 5 constitutes the conclusion for this thesis, a summary of the findings obtained from this investigation is presented and the scope of future research work is discussed briefly.

CHAPTER 2

LITERATURE REVIEW

In this chapter, a critical assessment of previous experimental and numerical investigations on the thermal properties of polymer based materials is presented. The first part of this chapter will focus on the review of thermal properties of amorphous materials, mainly for thermal conductivity and interfacial thermal conductance. The second part of this chapter will discuss various candidates as fillers for polymeric matrix. Due to the outstanding thermal, mechanical and electrical properties, carbon based material have been selected for discussion as primary fillers to improve polymeric materials. Lastly, Chapter 2 reviews the functionalization effect on thermal transport, which brings a broader vision of polymer application in electronics and thermal managements in the future.

2.1 Thermal Properties of Amorphous Polymer and Polymer Chain

2.1.1 Overview of Thermal Conductivity Calculation of Amorphous Polymer and Polymeric Chain

Phonon, the quantized particle of vibration, is the primary thermal energy carrier in most of the polymers. The thermal conductivity, *k*, of amorphous polymer is typically as low as 0.1-1.0 W/m-K at room temperature (see Table. 2). The numerous defects in amorphous polymers and its random structure results in intensive phonon scattering inside the polymer and low phonon mean free path. This is a primary reason for the low thermal conductivity of amorphous polymers [2, 14].

Multiple studies have used molecular dynamics (MD) simulations to explore the thermal conductivity of amorphous materials. The most general numerical method employed for thermal

transport study is non-equilibrium molecular dynamics (NEMD). Terao *et al.* [15] described method of reverse non-equilibrium molecular dynamics (RNEMD) to generate heat flux in samples by exchanging the particle velocities in different regions. The study also developed the Dual-Thermostat Method and Heat-Injection Method to obtain the linear temperature profile and then to calculate the thermal conductivity of amorphous polymeric materials. To reduce the statistical error of calculations, the Berendsen thermostat was introduced for the Dual-Thermostat Method, which can minimize the numerical errors of MD steps. For the Heat-Injection Method, the heat was added by the Langevin-noise term, but it was removed by a Berendsen thermostat. Similarly, after sufficient period to allow the system to reach steady state, the temperature profile was retrieved to calculate the thermal conductivity. Both methods were applied under periodic boundary conditions and the thermal conductivity was calculated as $k = \frac{1}{2S} \frac{\left\langle \left| \Delta E / \Delta t \right| \right\rangle}{\left\langle \left| dT\left(x\right) / dx \right| \right\rangle}$, where $\left| \Delta E / \Delta t \right|$ was the heat flow and $\left| dT\left(x\right) / dx \right|$ was the temperature gradient; S was the cross-section area. The example of thermal conductivity calculation for Polyamide 66 (PA66) was approximately 0.27±0.03 W/m-K, which was close to the experimental result of 0.25 W/m-K. Both methods are numerically efficient, and they could be used for different materials not just amorphous polymers.

The thermal conductivity of an amorphous polymer can be significantly dependent on the polymer chain length (CL, number of carbons in each single chain) [16]. A recent study addressed this issue by varying the CL from 4 to 1260 for polyethylene (PE) [17]. By applying the united-atom (UA) NEMD method, the thermal conductivities of PE were calculated as 0.004 to 0.11 W/m-K for CL in the range of 4 ~ 1260. The study concluded that the competition of collisions between beads and phonon vibrations determined the thermal conductivity of an

amorphous polymer with different CLs. While CL ≤ 7, collision between beads has dominant contribution to thermal conductivity because beads could move freely to collide with each other due to weak entanglement. For CL ≥ 140, phonon vibration was the major contribution to thermal conductivity since the entanglements between beads reduce their collision. The collision mechanism and phonon vibrations compete in their contribution to thermal conductivity of PE if $12 \leq CL \leq 140$.

Table 2. Summary of thermal conductivities of various types of amorphous polymer.

Adapted from Reference [2]

Material	Thermal Conductivity at 25°C (W/m-K)
Low density polyethylene (LDPE)	0.30
High density polyethylene (HDPE)	0.44
Polypropylene (PP)	0.11
Polystyrene (PS)	0.14
Polymethylmethacrylate (PMMA)	0.21
Nylon-6 (PA6)	0.25
Nylon-6.6 (PA66)	0.26
Poly(ethylene terephthalate) (PET)	0.15
Poly(butylene terephthalate) (PBT)	0.29
Polycarbonate (PC)	0.20
Poly(acrylonitrile-butadiene-styrene) copolymer (ABS)	0.33
Poly(ether ether ketone) (PEEK)	0.25
Polyphenylene sulfide (PPS)	0.30
Polysulfone (PSU)	0.22
Polyphenylsulfone (PPSU)	0.35
Polyvinyl chloride (PVC)	0.19
Polyvinylidene difluoride (PVDF)	0.19
Polytetrafluoroethylene (PTEE)	0.27
Poly(ethylene vinyl acetate) (EVA)	0.34
Polyimide, Thermoplastic (PI)	0.11
Poly(dimethylsiloxane) (PDMS)	0.25
Epoxy resin	0.19

Even though amorphous polymeric materials have low thermal conductivities, the single polymer chain exhibited high thermal conductivity [18, 19]. The polymer chain could be

modeled as a crystalline material with a single unit cell. According to Fermi, Pasta, and Ulam's (FPU) study, thermal conductivity could diverge and tend to infinity for 1D anharmonic oscillators [20]. A study by *Henry et al.* [21, 22] reveal that the polymer chain of Polyethylene (PE) had exceptionally high thermal conductivity (~ 350 W/m-K) for a chain with 40 unit cells but could be even higher for different polymers. *Henry et al.* [21] used Green Kubo (GK) relation and modal analysis, in MD simulations, to determine the thermal conductivity of PE chains. The relaxation time of a single chain was also calculated by using the normal mode decomposition technique [23, 24] and used in Boltzmann Transport Equations based calculations to estimate thermal conductivity. The final results for PE chain of different lengths and different cases were shown in Figure 2.

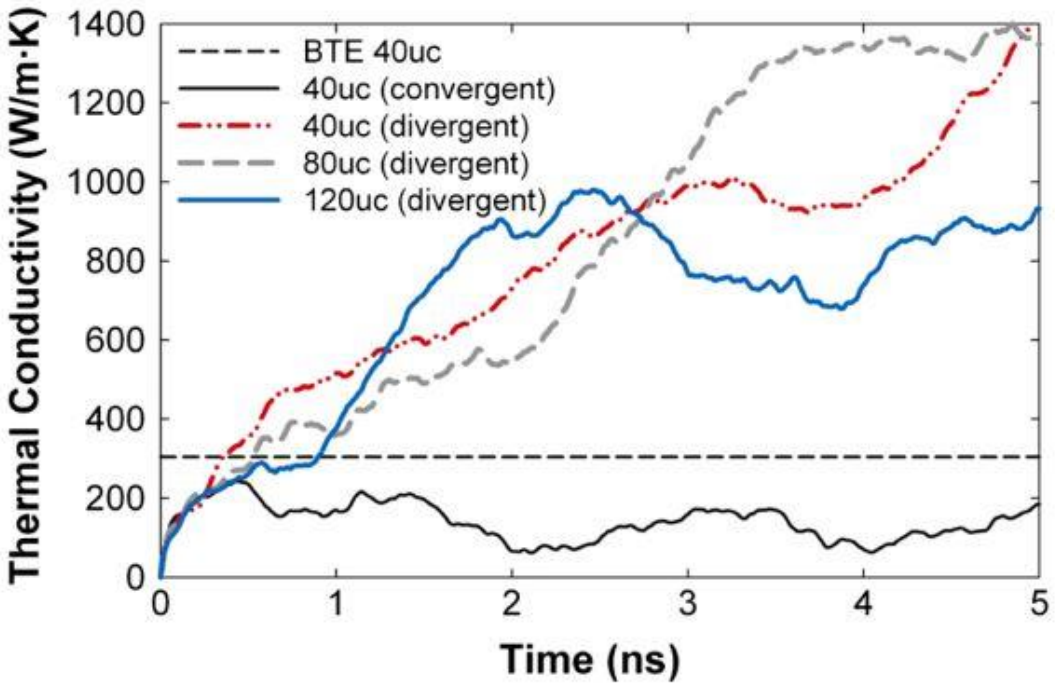

Figure 2: Thermal conductivities of polymer chain of Polyethylene in different lengths measured by unit cells (UC). Besides one result labeled by BTE, other results were obtained by integration of Heat Current Autocorrelation Function (HCAF) calculated by MD up to 5ns. Adapted from Reference [21]

Henry et al. observed divergence in thermal conductivities for some chains using GK calculations but the reason for divergence could not be identified easily. The divergence of thermal conductivities resulted from a divergence of Heat Autocorrelation Function (HACF) with time. For highly nonlinear systems, interpretation of diverging HACF can be complicated.

The anharmonicity [25] is the reason for finite thermal conductivity of materials. The fundamental of lattice dynamics conflicted with the observation of infinite thermal conductivity by FPU hypothesis [22]. To continue seeking the reason why the thermal conductivity of PE chain tend to infinity, Henry *et al.* extended the GK model by incorporating a normal mode-mode correlation function in MD [22]. Henry *et al.* explained that, the individual atomic motion in idealized perfectly harmonic crystal was independent of each other. Compared with 3-D perfect harmonic crystal, the allowable scattering events were significantly reduced in 1-D chain. In such situation, many phonons were non-interacting and the phonon-phonon scattering events did not exist. Henry *et al.* suggested that the phonon-phonon scattering events in 1-D chain could be cross-correlated temporally, which led to additional contribution of heat conduction. If a system of phonons had sequenced and recurrently occurring phonon-phonon scattering events, the mode-mode cross correlations would exist in the system and the anomalous heat conduction could occur in the system. They performed model analysis and observed that the optical modes correlation decay time was very short compared with the acoustic mode correlations, and they did not contribute much to the thermal conductivity of a polymer chain. Longitudinal acoustic mode (LA) modes played important role in the contribution to thermal conductivity (on the order ~100 W/m-K). There was a strong divergence for LA mode-mode correlations in some of the calculations. Although not all LA mode-mode correlations show divergent phenomena in 1-D

systems, the divergence of some modes are significant leading to the divergence of thermal conductivity.

NEMD was also extensively applied for thermal conductivity calculation of polymer chains, polymer film based on polymer chain confinement and crystalline polymer [19, 26, 27]. Liu *et al.* [19] focused on the thermal conductivity of polymer chains and phonon scattering mechanisms. By setting up slabs of hot and cold regions, the heat flux was calculated and then thermal conductivity was determined. The study emphasized that the thermal conductivity of aromatic-backbone structures was higher than that of aliphatic-backbone structures. The comparison between poly (*p*-phenylene), polybenzimid (aromatic-backbone) and polyethylene (aliphatic-backbone) was performed. In general, the thermal conductivity would increase as the stiffness increased. Aromatic-backbone structures were stiffer than aphalitic-backbone structures because of sp^2 hybridization. Besides the backbone structure, bonding strength was a factor to influence the thermal conductivity. The thermal conductivity of a polyacetylene chain (double carbon-carbon bonds) could be up to 2.6 times that of a polyethylene chain (single carbon-carbon bond). However, the bond-strength disorder, mass disorder, and mixing with non-original atoms in the chain would cause significant lower thermal conductivity. The phonon-boundary scattering relaxation time, τ_1, and intrinsic phonon relaxation time, τ_2, were discussed for different types of backbone structures in [19]. Phonon boundary scatterings dominated the scattering mechanisms in short chain (unit-cells < 100), and intrinsic phonon scatterings dominated in long chain (unit-cells > 200) for both aphalitic- and aromatic-backbone structures. However, for disordered backbone structures (mass disorder or bond-strength disorder), intrinsic phonon scattering always dominated the scattering mechanisms. However, this study did not discuss the divergence and convergence factors for thermal conductivity of polymer chains.

Comparing the GK method and the NEMD method for computing thermal conductivity of polymer chains, the GK method is more practical for simulation based on its natural incorporation of periodic boundary conditions, as smaller computational domains may work fine. For the NEMD method, the temperature or heat flux applied on regions would introduce artificial phonon scatterings, and the size effect (due to long mean-free path of phonon inside polymer chain) might make the computational cost expensive.

2.1.2 Phonon Modeling for Disordered Materials

The vibrational properties of disordered system are characterized as extended particles (extendons) and localized particles (locons) [28]. Extendons can be divided into propagons and diffusons. Allen *et Al.* [28] took amorphous silicon as an example to determine the frequency range for locons and extendons in the vibrational spectrum. Propagons, the phonon-like particles in disordered materials, were located at the low frequency domain and had the ability to travel at least 2-3 interatomic distances before scattering. Based on this, the mean free path could be defined for propagons. As the frequency increased, there was a boundary named the Ioffe-Regel crossover between the regions of diffusons and propagons. The study showed that 4% of the spectrum was composed of propagons and diffusons fill 93% of the spectrum. Unlike propagons, diffusons did not propagate in the same direction, which made it hard to define their wavevector. There was a mobility edge between diffusons and locons in the high frequency region. And diffusons drop to zero at the mobility edge. Locons had less mobility than propagons and diffusons, thus could be considered as static. The model proposed in the study by Phillip B. Allen [28, 29] to calculate thermal conductivity was derived from the Green Kubo formula and based on harmonic approximation relation. Interestingly, the thermal conductivity of propagon

modes converged after a “plateau” region (5-30K), but that of diffuson modes kept increasing to about 100K. The conclusion of this study was that diffuson modes contributed to the thermal conductivity of amorphous silicon significantly at high temperature due to the high diffusivity of diffuson modes in the Green Kubo formula and harmonic approximation relation. Researchers from Dr. Henry’s group extracted the information for each mode of propagons and diffusons to study in detail the thermal properties of amorphous silica, which would illuminate the exploration of amorphous materials [30].

The virtual crystal approximations (VC) method of modeling disordered materials was comparable to the method of identifying different traveling particles. Larkin, *et al.* (2013) [31] combined the VC anharmonic lattice dynamics (ALD) method, MD-GK and MD normal mode decomposition technique simulations to explore the thermal properties of alloy materials. Lennard-Jones (LJ) argon (Ar) and Stillinger-Weber (SW) silicon (Si) were used considered in the simulations. The first step of the overall simulation was to apply VC to model the alloy as a crystalline material. In brief, the disordered supercell was created by different isotopes of Si and Ar, and VC remodels the supercell by averaging the mass and by using DFT to calculate the force constant between atoms. To verify whether the modeling was successful or not, normal mode decomposition technique (NMD) in MD [24, 32] was employed to compute the phonon lifetime for supercells and VC-unit cells, and both results had same trend and magnitude for phonon lifetimes. Thermal conductivities are calculated by GK, VC-ALD, VC-NMD. The results by those methods were similar [31, 32].

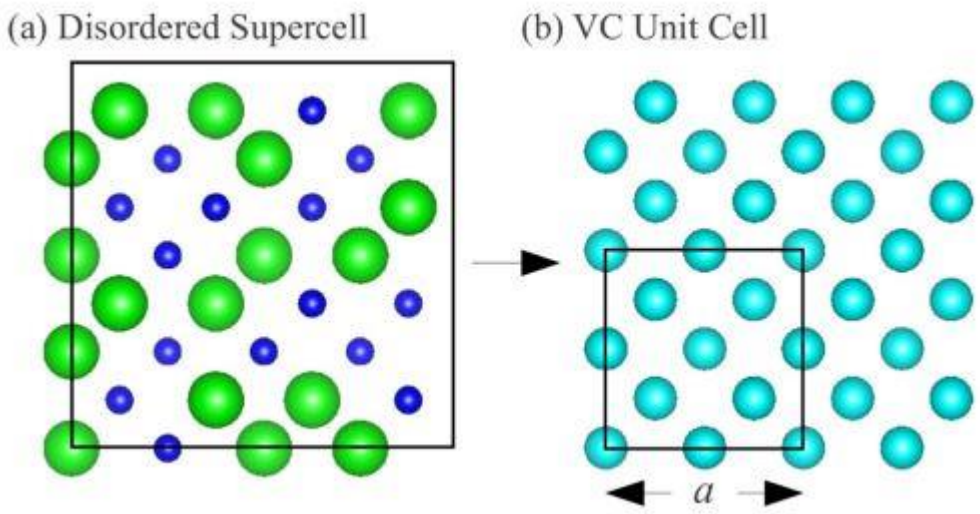

Figure 3: Virtual crystal approximation for disordered supercell of silicon. Adapted from Reference [27]

2.2 Carbon Based Fillers/Polymer Nanocomposite

Carbon nanotube (CNT), graphene and graphite were popular carbon based nanomaterials that showed excellent thermal, electrical and mechanical properties [2]. This section reviews the thermal properties of carbon based fillers. Study in [33] reviewed the thermal conductivities of different fillers, which were summarized in Table 3.

Table 3. Summary of thermal conductivities of fillers for amorphous polymer. Adapted from Reference [2].

Material	Thermal Conductivity at 25°C (W/m-K)
Graphite	100 ~ 400 (on plane)
Carbon black	6 ~ 174
Carbon Nanotubes (CNTs)	2000 ~ 6000
Diamond	2000
PNA-based Carbon Fibre	8 ~ 70 (along the axis)
Pitch-based Carbon Fibre	530 ~ 1100 (along the axis)
Copper	483
Silver	450
Gold	345
Aluminum	204
Nikel	158
Boron Nitride	250 ~ 300
Aluminum nitride	200
Beryllium oxide	260
Aluminum nitride	20 ~ 29

Specifically, the thermal conductivity of a CNT could be up to 6600 W/m-K at 300K from calculations in [34]. The thermal conductivity of a suspended single layer graphene was estimated in the range of $\sim$ $(4.84 \pm 0.44) \times 10^3$ to $(5.30 \pm 0.48) \times 10^3$ W/m-K at room temperature from Raman *G* peak frequency on the excitation laser power [35, 36]. In recent decades, single-walled CNT (SWCNT) and graphene had been modeled as functional materials for thermal management, and electronic devices such as CNT based thin film transistors. [18, 37-39].

2.2.1 Review of Fillers for Polymeric Nanocomposites

Polymeric nanocomposites were strong candidates for applications in electronics, aerospace and medical devices; highly conductive materials were used to improve polymeric properties. Combined with light weight, the improved thermal and electrical properties attracted

high attention from scientists [4, 33, 40, 41]. Researchers have considered multiple types of fillers for polymeric matrices.

Metallic particles would increase the thermal and electrical properties of the composites. However, the high density of metal might not be the ideal candidate for fillers, which limited the potential of metallic fillers when light weight was requested. Copper, nickel and aluminum have been used as fillers in previous investigations [7, 42, 43]. Ceramic fillers, such as aluminum nitride (AlN), boron nitride (BN) and silicon carbide (SiC), were added to polymer as powder to increase the thermal conductivity of a composite. However, the electrical resistivity of the composite also increased. While it was necessary to improve both thermal conductivity and electrical conductivity at the same time, and ceramic maintained the light weight needed for usage, metallic and ceramic fillers would not satisfy the requirements [44-46].

Since carbon-based fillers were materials with high thermal and electrical conductivities, and light weight, they were promising candidates for improving the properties of polymeric composites. The traditional carbon-based fillers were carbon black and carbon fibers. Carbon black had been found to be significantly contributed to electrical conductivity, and carbon fibers had been reported to have high thermal conductivity in the axial direction (~2000 W/m-K) but low thermal conductivity (~10-110 W/m-K) in the transverse direction. This would affect the transverse thermal conductivity of an aligned axial composite. Novel carbon-based fillers, such as carbon nanotube (CNT), graphene and graphite, exhibit not just great thermal properties but excellent electrical and mechanical properties as well [4]. Recently, CNT was actively researched as the most popular filler for polymeric materials, such as amorphous polyethylene, paraffin, epoxy and amorphous argon [47-51]. Those studies [11, 12, 48, 52, 53] revealed that the thermal conductivity of a composite increased as the CNT was filled inside polymer matrix.

The Maxwell-Garnett Theorem for effective thermal conductivity predicted the transverse and longitudinal components of the composite conductivity. The volume fraction of fillers might change the effective thermal conductivity significantly. S. Hida *et al.* [49] displays the results for CNT-polyethylene composite, which suggested that the composite thermal conductivity could be six times that of the original polymer matrix. A similar simulation from Y. Kuang *et al.* [48] also mentioned that the MWCNT might increase the composite thermal conductivity much greater than SWCNT. When MWCNT or SWCNT was filled inside the polymer matrix, thermal conductivity of composite increased as the temperature of composite increased. Y. Kuang *et al.* also performed the theoretical calculations to estimate the composite thermal conductivity and confirmed that the results might vary due to size effects of composite. In the review paper [33, 54], the effective medium theory for thermal conductivity of polymeric composite were discussed. NEMD simulations may not be the best choice for the calculation of the CNT thermal conductivity since there were issues for parameters of potential and simulation length of model. Multiple studies [34, 55-57] showed different results and they were in the range of $10^2 \sim 10^3$ W/m-K), which may be due to the issues with size of the computational domain and potentials as mentioned above [58-62]. Additionally, the experimental results are much lower than the simulation results. One reason could be the non-straightness of CNTs inside polymer matrices during fabrication processes, which would reduce the values of composite thermal conductivity [33].

2.2.2 Interfacial thermal Transport between Carbon Based Materials and Amorphous Materials

Many experimental and simulation studies reported the interfacial thermal boundary resistance between carbon-based and disordered materials. Such studies are very important for thermal management of electronic devices and manufacturing. In summary, there were three typical configurations used for analyzing thermal interaction between carbon based and amorphous materials.

1) Carbon based materials supported on substrate

The cases of interface thermal transport between supported CNT/graphene and a-SiO_2 (amorphous SiO_2) substrate were studied in Refs. [63-66]. Most of the studies discussed the phonon coupling of CNT/graphene and a-SiO_2, and reveal that the phonon life time significantly reduced compared to the suspended CNT/graphene, as strong scattering occurred at the interface [63, 64]. Specifically, the strong low frequency phonon scatterings were noticeable for CNT/a-SiO_2 devices. In the high frequency region, the optical phonons dominate energy transport, and they are strongly coupled with electrons. Consequently, the optical phonons are important for hot electrons energy relaxation [64].

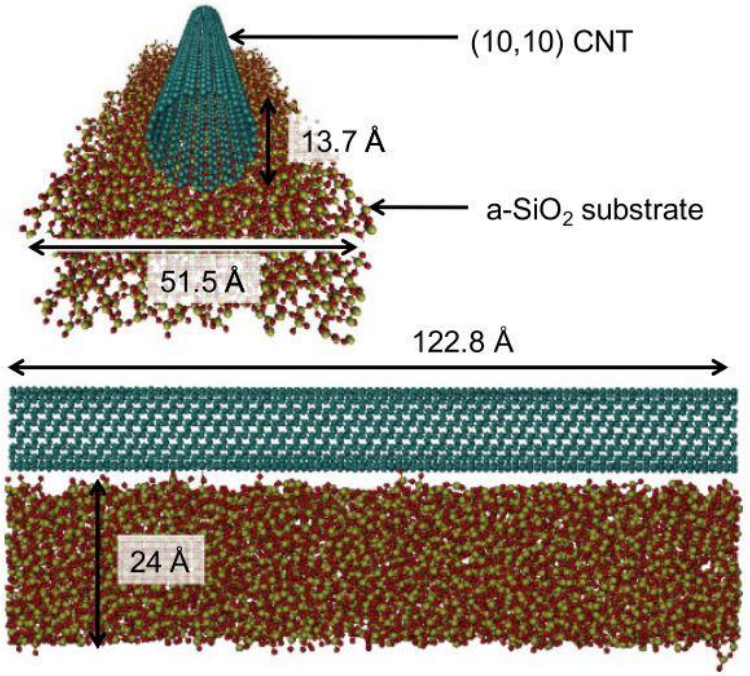

Figure 4: Model of SWCNT on a-SiO_2 substrate. Adapted from Reference [45].

Z. Ong *et al.* [65] presented simulations for varying CNT-a-SiO_2 interaction strength by changing a related parameter, χ , in the Lennard-Jones potential. While the coupling strength was greater, the thermal boundary conductance (TBC) between CNT and the substrate was higher. Three cases of (6,6), (8,8) and (12,12) CNTs were considered to study the diameter dependence of the TBC. This showed that larger diameter (greater chirality number) CNTs would enhance the TBC between CNT and a-SiO_2.

2) Sandwiched Structure

T. Luo *et al.* [67] studied thermal transport at the interface of graphene/graphite and polymer matrices using a NEMD method with different potentials, including Lenard-Jones (L-J), adaptive intermolecular reactive empirical bond order (AIREBO) potential and condensed-phase optimized molecular potentials for atomistic simulation studies (COMPASS). As the figure

showed, a single graphene layer is sandwiched between two amorphous polymeric matrices (paraffin wax, $C_{30}H_{62}$); there were two fixed layers at both edges of the model as heat source and heat sink. To maintain the temperature difference along the composite, a Langevin thermostat was used in the MD simulation to achieve the steady state for the system. A temperature difference exists at the center of the system, and the TBC is calculated as $J / \Delta T$, where J was the heat flux and ΔT was the temperature difference. The TBC did not change significantly, while the lengths of the polymer blocks on the two sides of the graphene changed (~61-62 MW/m^2-K). However, as the cross-section area of the composite increased, the TBC changed from 61 MW/m^2-K to its saturated value (~71 MW/m^2-K).

The following model of graphite between two polymer blocks was analyzed by a similar method. However, the TBC found in this case was approximately 30-32 MW/m^2-K, which was smaller than that of graphene. The researchers also examined the effect of covalent bonding between graphite and polymer on TBC. The result was that TBC increased to 35 MW/m^2-K. This result implied that a stronger interaction between graphite and polymer matrices on both sides could be useful to achieve better thermal performance. To investigate thermal coupling between graphene and paraffin wax, the phonon spectra were calculated for both graphene and amorphous paraffin wax. The study explained that the overlapped regions of spectra for graphene and paraffin wax in the range of 2 to 16 THz, which means that graphene out-of-plane would be more important for thermal coupling with paraffin wax.

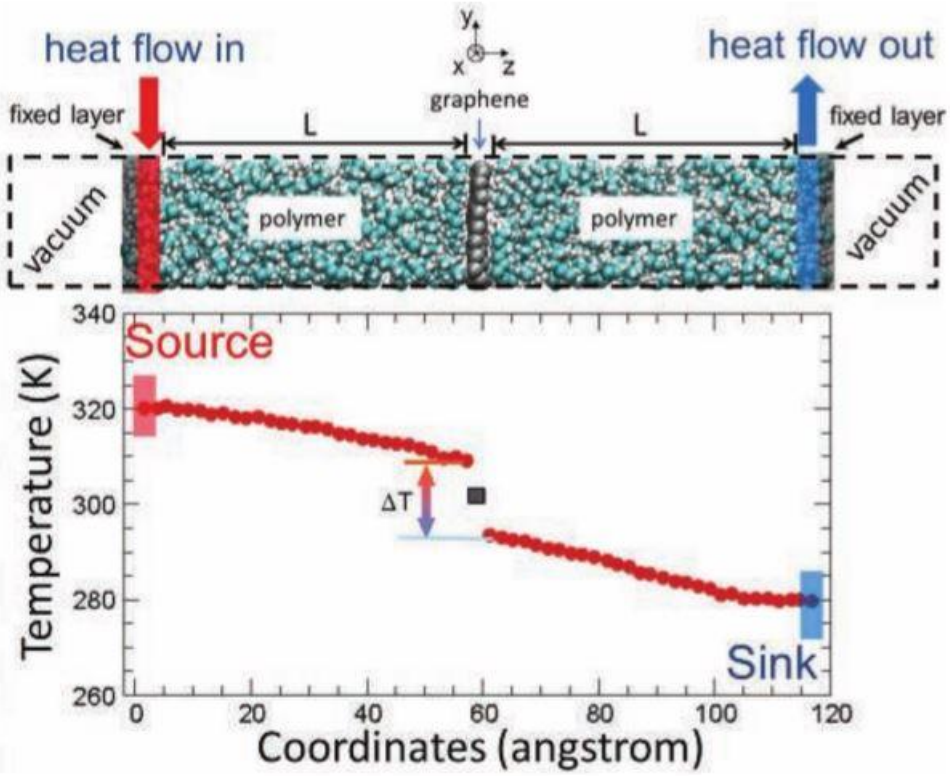

Figure 5: A system setup and an example steady state temperature profile of the polymer-graphene junction. Adapted from Reference [47]

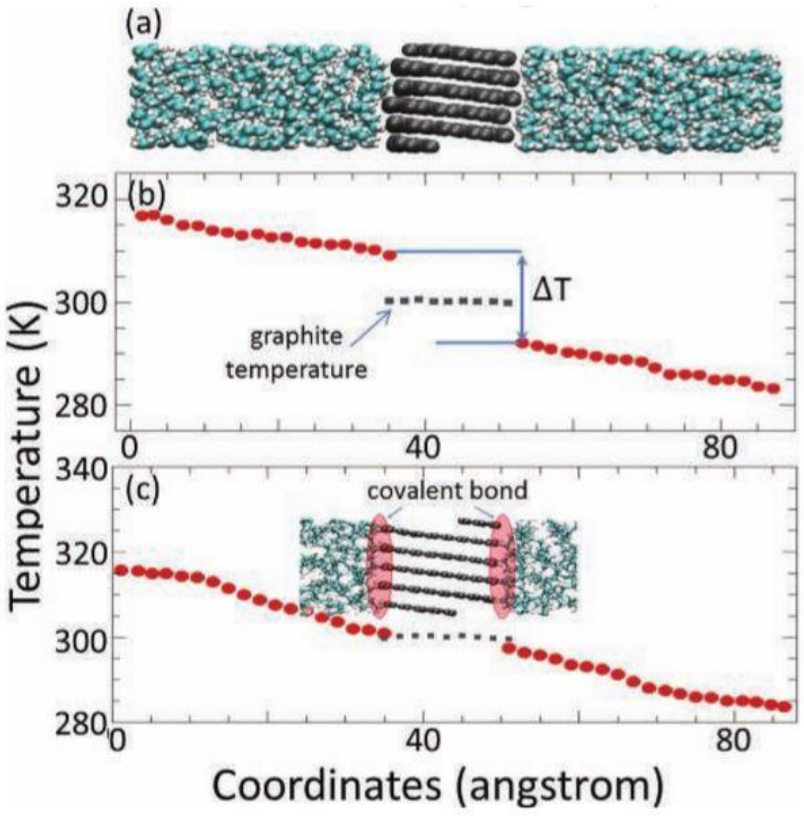

Figure 6: A simulation setup of a graphite-polymer junction and temperature profile. Adapted from Reference [47]

3) Carbon based fillers embedded in polymer matrices

Many recent studies on carbon based fillers in polymer surrounding matrices concentrate on CNTs [11, 12, 47-50, 54, 68-70]. The thermal properties and electrical properties of CNTs were comparable to graphene. Most of the studies were concerned with the calculation of the Kapitza resistance (the inverse of thermal boundary conductance) between CNT and polymeric matrices. *S. Hida et al.* showed that the phonon lifetimes of CNTs are suppressed while it was embedded inside a polymeric matrix, especially in the low frequency region. This phenomenon was similar to the model of supported CNTs by substrate due to the phonon scattering at the

boundary. Kapitza resistances for different cases of CNT/polymer matrix are summarized in the table below:

Table. 4 Summary of Kapitza Resistances of CNT/Polymer Composite

Literature Studies	Kapitza Resistance (m^2-K/W)
S. Hida et al.(CNT-polyethylene)	6.54×10^{-8} (theoretical)
Y. Kuang et al. (CNT-polyethylene)	1.60×10^{-8} (theoretical)
Huxtable et al. (CNT-octane)	4.00×10^{-8} (theoretical)
Shenogin et al. (CNT-octane)	3.30×10^{-8} (theoretical)
Clancy et al. (CNT-polymer)	$0.20\text{-}9.60 \times 10^{-8}$ (theoretical)
Carlborg et al. (CNT-argon)	40.0, 62.5×10^{-8} (theoretical)
Brying et al. (CNT-epoxy)	$0.24\text{-}2.6 \times 10^{-8}$ (experimental)
Varshney et al. (CNT-epoxy)	$0.77\text{-}2.5 \times 10^{-8}$ (theoretical)

Most of those results were calculated by the NEMD method and the transient relaxation method (both of them will be introduced in Chapter 3). However, there was a difference of about 10-40% between these two methods for a given case study. The simulation studies listed in table above did not examine whether the results of TBC were reasonable or not, since they only used either transient relaxation method or NEMD method to calculate Kapitza resistance.

2.3 Functionalization Effects and Crosslinks for Thermal Transport

2.3.1 Experimental Studies for Thermal Transport

As the previous section had discussed, polymer chains had higher thermal conductivities compared to amorphous polymer. *G. Kim et al.* [71] and *V. Singh et al.* [72] engineered the

amorphous polymer chains and their interactions to enhance the thermal conductivity of the bulk polymer. *G. Kim et al.* used four different types of polymer materials to observe the thermal conductivity of a modified structure. Poly (N-acryloyl piperidine) (PAP) was the H-bond-accepting polymer, while the other 3 types of polymers are H-bond-donating materials: poly (acrylic acid) (PAA), poly (vinyl alcohol) (PVA) and poly (4-vinyl phenol) (PVPh). PAP played the role as side chain placed with long chain polymer PAA, PVA and PVPh together. Here, the researchers emphasized that the carboxylic acid (-COOH) in PAA and the phenol (-PhOH) in PVPh had stronger power to donate H atom than the functional group (-OH) in PVA, which would bring different effects of changing the thermal conductivity of the structure. While PAP and PAA polymer chains were connected together, thermal conductivity had a huge improvement ($\geq$ 1.5 W/m-K), which was almost ten times that of amorphous PAA and amorphous PAP. However, even the PVPh also had higher power of H-bond-donating, the measured thermal conductivity of PAP-PVPh was approximately 0.2 W/m-K. This performance was even lower than PAP-PVA (0.2-0.4 W/m-K). For both PAP-PAA and PAP-PVA cases, thermal conductivity reached its maximum value while the concentration of PAP is around 0.3.

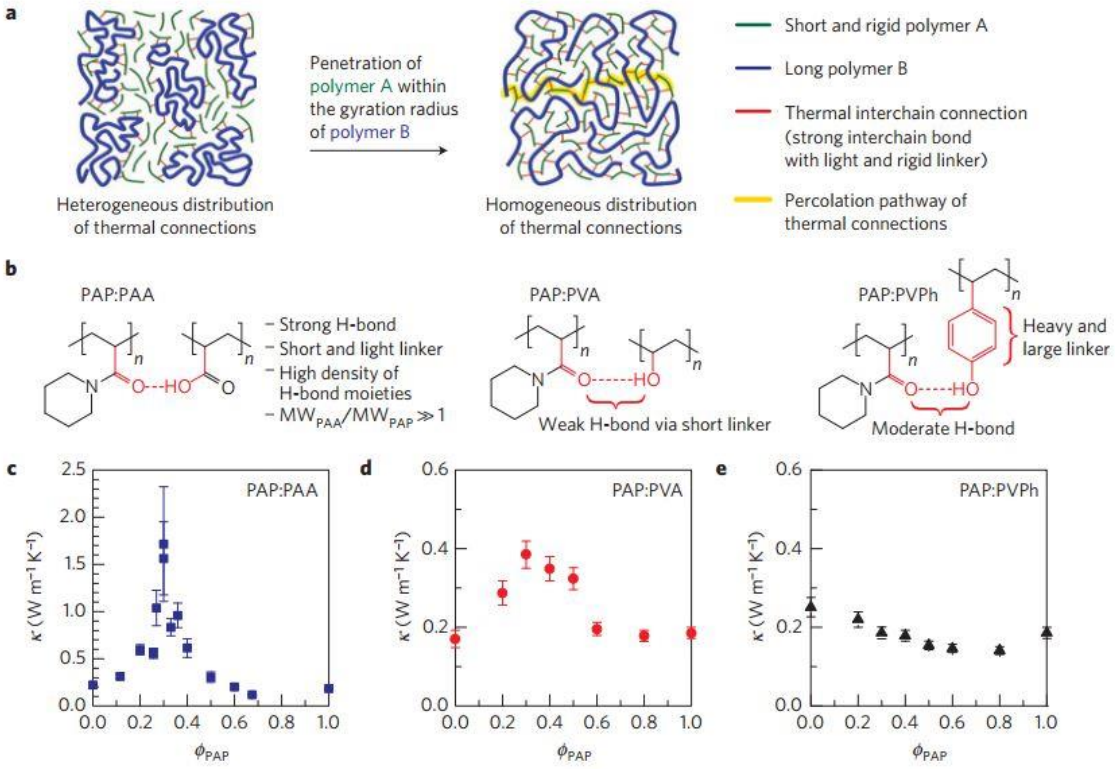

Figure 7: High thermal conductivity in amorphous polymer blends by engineered interchain interaction with different functional groups [52]

V. Singh et al. [72] designed polymer chains that aligned in the same direction by using plate-assisted electropolymerization. The sample polymer for this study was polythiophene. The measured thermal conductivity was 20 times greater than of the bulk polymer, e.g., 4.4 ± 0.3 W/m-K. The study also used equilibrium MD simulation to observe the thermal conductivity of a single polythiophene chain. The calculated thermal conductivity was much higher than the results of the measurement. This suggested that the phonon transport along the single chain would be responsible for the enhancement of thermal conductivity. *M. Losego et al.* [73] reported that the interfacial thermal boundary conductance (TBC) increased between gold film and a Qz substrate when self-assembled monolayers (SAMs) was introduced between them. The

SAM was formed by a layer of crosslinks with different types of functional groups. Overall, as the SAM (crosslinking layer) was bonded with the gold film layer and the Qz substrate, the TBC between them reached its highest value of 65 MW/m^2-K while the density of covalent bonds increased to the limit.

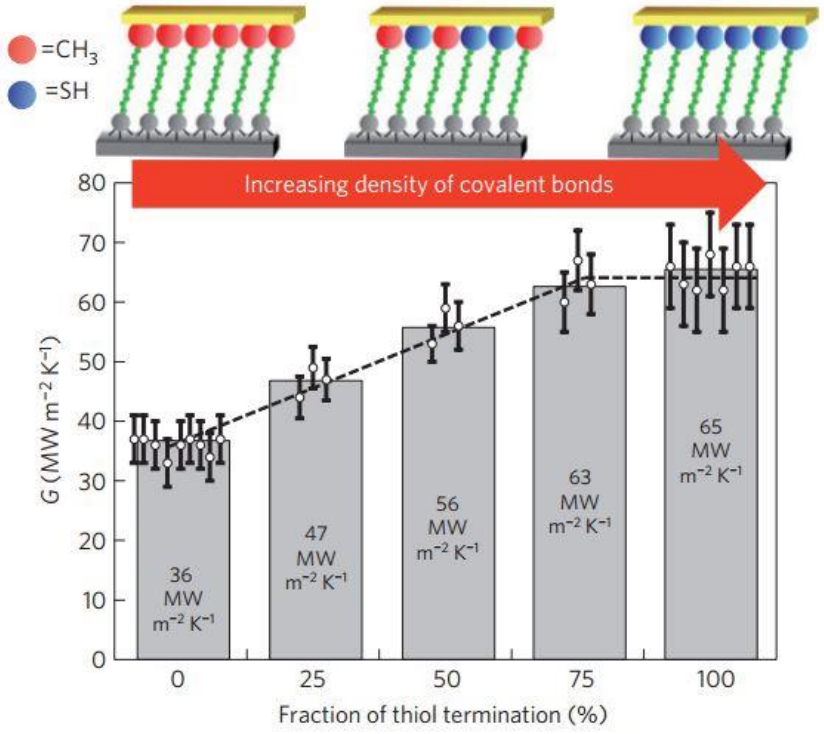

Figure 8: Interfacial thermal conductance between gold film layer and z-cut quartz (Qz) with increasing density of covalent bonds [54].

The following discussion is about the functionalization of CNTs. *Gulotty et al.* [41] indicated that Carboxylic acid (-COOH) functionalized on SWCNT and MWCNT would increase the dispersion properties so that they could improve the CNT-polymer nanocomposite electrical and thermal conductivities. Comparing the loading fraction (wt%) of CNTs to improve electrical conductivity of the composite (~1 wt%), improvement in thermal conductivity requires much higher loading fraction (~3wt%). Measurements results by Gulptty *et al.* [41] predicted

that the thermal conductivity of a composite with functionalized CNTs could increase by about 25%. However, the measured thermal conductivity of functionalized CNT decreased because functionalization created side wall defects that impeded acoustic phonon transport along CNT.

Since carboxylic acid (-COOH) group could be functionalized on the surfaces of SWCNT and MWCNT, Choi *et al*. [74, 75] introduced in-situ polymerization experiments for grafting of poly (ether ketone) onto MWCNT. They demonstrated that PEK could be grafted on the surfaces of CNTs following Friedel-Crafts Acylation in Phenoxybenzoic acid (4-PBA) and Poly(phosphoric acid) (PPA) environment. Moon *et al*. [13] used steady state DC thermal bridge method to measure the thermal conductivity of PEK/CNT for different weight ratio (wt%) of CNT cases. At 400 K temperature and CNT wt% of 28%, the thermal conductivity of PEK/CNT fiber was measured as 35 W/m-K. The measurements revealed that thermal conductivity of PEK/CNT fiber with the loading wt% below 20% did not increase as the temperature increased. However, as loading wt% of CNT increased to 28%, thermal conductivity increased with increase in temperature.

2.3.2 Recent Simulation Studies of Crosslinking

Simulation studies on the effects of functionalization gave a more profound understanding of the impact of crosslinking on thermal transport. Single layer graphene was known for its excellent thermal properties, due to strong C-C sp^2 covalent bonds. However, the interactions between adjacent graphene layers spaced 3.35Å was dominated by the van der Waals force; the in-plane thermal conductivity was ~3000 W/m-K and the out-of-plane thermal conductivity was ~50 W/m-K. This behavior limited the thermal transport between graphene sheets. While the C-C bonding strength is 2 orders of magnitude higher than van der Waals

interactions, it could be the key to solve the low performance of interfacial thermal transport between graphene sheets. *Liu et al.* [76] applies (-CH_2-CH_2-) crosslinks between 2 graphene sheets and employed the Lenard-Jones potential in NEMD to analyze the TBC. The figure shown below was the structure of 2 single layer graphene sheets. The overlapped region was functionalized by the (-CH_2-CH_2-) crosslinks. The value of the TBC increased greatly as the number of crosslinks increased. The cases of this study include 0, 3, 15, 24 crosslinks. The behavior of a random spatial arrangement of crosslinks did not have any obvious difference with the regular arrangement of crosslinks. Finally the phonon spectra of carbon atoms in crosslinks and out-of-plane graphene were overlapped in the low frequency region, which meant that the heat transfer in this region was efficient for out-of-plane graphene phonon modes.

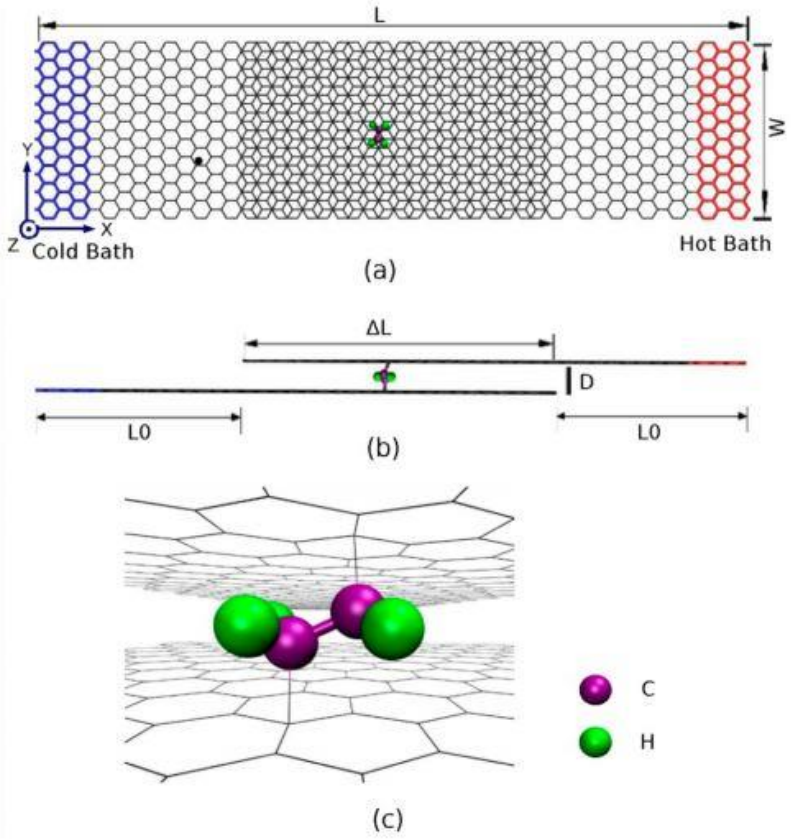

Figure 9: Schematic of a graphene junction with a single covalent cross-linker: a) top view; b) side view; c) the covalent cross-linker between two graphene sheets [56].

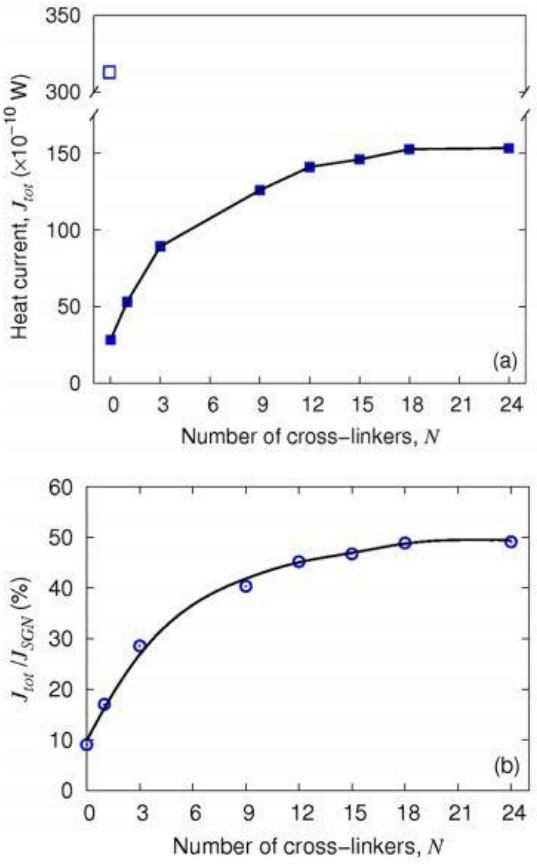

Figure 10: Heat current passing through the junction as a function of the number of cross-linkers N, and the ratio of heat current passing through the junction to that passing through a monolayer freestanding graphene with same size. [56]

Varshney et al. [47, 68] studied the effect of functionalization on CNT for epoxy composites. The results by NEMD simulations also showed that increasing functionalization degree would enhance the TBC. Also, the TBC at the interface of the crosslinked matrix and functionalized CNT was higher than the TBC of uncrosslinked matrix with functionalized CNT.

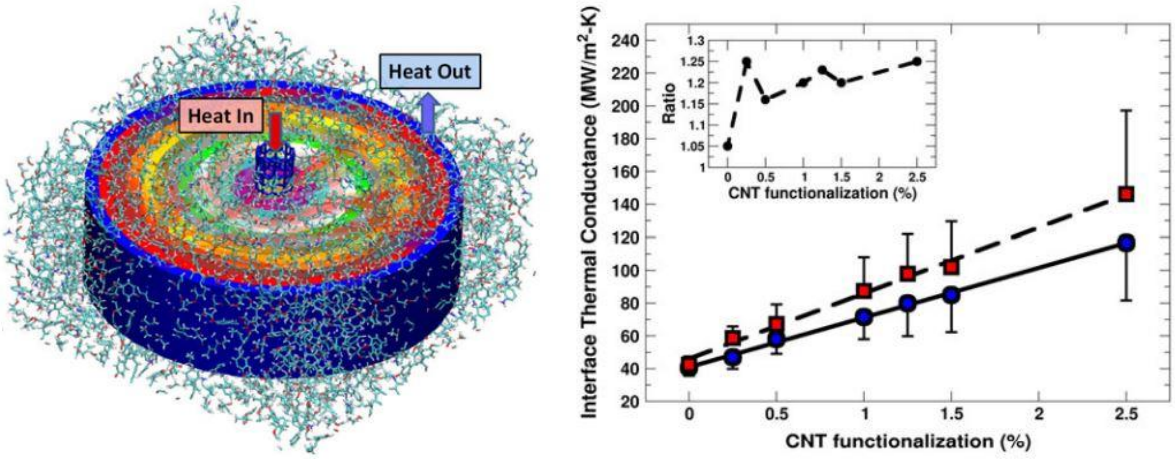

Figure 11: Schematic of division of CNT-epoxy matrix system in MD simulation; Interface thermal conductance for functionalization degree 0-2.5% [38].

Wang *et al*. [77] applied NEMD to study TBC between graphene and paraffin as different functional groups, e.g., butyl, methyl, phenyl, formyl, carboxyl, amines and hydroxyl covalently functionalized on pristine graphene. While the degree of functionalization (%) increases, the TBC decreased and converged at ~6.0%. Different functional groups had different spectra and overlapping of the spectra between graphene and functional groups affect the energy transfer. Butyl has good spectra overlap with the majority of spectra of pristine graphene, and it was found that butyl was the most efficient functional group for enhancing energy transfer from graphene to paraffin. However, the change in number of graphene layers at the interface between graphene and paraffin did not have significant contribution to the reduction of interfacial thermal resistance. In another study, Wang *et al*. [78] changed the length of polyethylene crosslinks functionalized on pristine graphene, used NEMD simulations, and found that the TBC increased as the length of crosslinks increased. Wang *et al*. [78] also found that the TBC increased with the functionalization degree.

In summary, Chapter 2 reviews previous literature, including experiments and simulations. Even though amorphous polymers had low thermal conductivities, polymer chains showed high thermal conductivities in both experiments and simulations. And length of polymer chains inside amorphous polymers could significantly affect thermal conductivity. The polymeric nanocomposites, with carbon based nanostructured materials embedded inside, exhibited excellent thermal properties. When crosslinks are made between carbon based nanostructured materials and polymer, TBC significantly increased. Even though few studies reported the results of functionalization effect on TBC between graphene/CNTs and polymers using numerical simulations, they did not explore the mechanism of phonon transport in detail. Most of them did not have solid experimental background to support numerical results. Experimental results shows that fiber spun from PEK functionalized CNT could improve the thermal conductivity by two orders of magnitude, but any numerical study has not been performed to understand the TBC at interface of CNT/PEK, the effect of functionalization and underlying thermal transport mechanism. Performing such study is focus of this thesis. Our simulations will study the TBC between CNT and PEK for different number of cross-links, and investigate phonon transport at interface using spectral energy density (SED) and spectral temperature in following chapters.

CHAPTER 3

COMPUTATIONAL METHODOLOGY

In Chapter 3, the first part will introduce the consistent valence force field (CVFF) for molecular dynamics (MD) simulations throughout this study. After that, the method of creating the amorphous poly (ether-ketone) (PEK) matrix is illustrated in details. The procedure of generating crosslinked SWCNT is the most important section in the 1st part. It is based on the observation of chemical reaction of hyperbranched carboxylic acids grafted on SWCNT/MWCNT from previous literature. The second part of this chapter will explain the calculation of thermal boundary conductance (TBC) between SWCNT and PEK matrix. The TBC will be computed by NEMD method (direct method). The last part of this chapter will present the spectral analysis formulation, which consists of spectral energy density (SED) method, transient spectrum and spectral temperature calculations.

3. 1 Structure Preparation by Molecular Dynamics (MD) Simulations

3.1.1 Consistent Valence Force Field (CVFF)

Multiple types of force field can be applied for molecular dynamics (MD) simulations, such as polymer consistent force field (PCFF), Assisted Model Building with Energy Refinement (AMBER) force field, Condensed-phase Optimized Molecular Potentials for Atomistic Simulation Studies (COMPASS) [67, 79]. Most of the consistent force field potentials are applied for polymers and biological systems MD simulation based on the experimental data and its definition of angle, bonding, dihedrals and impropers [80-82]. Recent years, material scientists studied molecular mechanics of CNT incorporated with force field potential so that the

mechanical properties (Young's Modulus) of CNT can be predicted accurately [83, 84]. In general, the expression of force field potential consists of energy of bonded portion and nonbonded portion. The bonded energy includes bonding, angle, dihedral and impropers between bonded atoms; and the nonbonded energy includes van der Waals interaction and electrostatic energy. The equation of force field potential is summarized as:

$$E_{tot} = E_{bond} + E_{angle} + E_{dihedral} + E_{impropers} + E_{vdw} + E_{coulombic} \quad (1)$$

Consistent valence force field (CVFF) is chosen for all the simulations. The reason to use CVFF is that it can predict the thermal properties such as thermal conductivity, thermal expansion, as other studies mentioned previously, which has a good agreement with the experimental results [47, 83]. As the previous studies mentioned, the long-range electrostatic term in CVFF can be simulated as particle-particle-particle-mesh (PPPM) technique and it is under error tolerance 1.0e-6 [47]. Under the CVFF, the design of material system is double-walled CNT (DWCNT) embedded in amorphous PEK. (Details of equations of CVFF potential expression and coefficients is explained in Appendix A)

3.1.2 Structure Preparation of CNT/PEK nanocomposite

In this study, the simulation domain consists of a (20, 20) CNT of length 39Å (~ 9 unit cells) embedded in a periodic amorphous PEK matrix of same dimension along the CNT axis. We use consistent valence force field (CVFF) for all the simulations and results reported in the present work. CVFF has been widely used to model amorphous polymeric systems, to predict their structural and thermal properties, and to model interface properties (such as TBC) at CNT-

filler based composites [47, 83]. The long-range electrostatic interactions in PEK are considered using particle-particle-particle-mesh (PPPM) technique with energy tolerance of 1.0e-6 [47].

In order to prepare the CNT/PEK nanocomposite, a single PEK chain with repeat units 2 ($C_{26}H_{18}O_5$) is first prepared using Materials Studio package and replicated 625 times using molecular dynamics package LAMMPS to make a slab of 30625 atoms. The slab was heated at high temperature of 1000 K and then rapidly quenched to make the amorphous structure. Thereafter, the polymer matrix was equilibrated in a series of NPT (1 atm; 300K), NVT (300K) and NVE ensembles.

To incorporate (20,20) CNT into PEK matrix, a cylindrical hole was constructed at the center of amorphous PEK matrix using LAMMPS fix-indent module. The CNT was then embedded in the central region of the amorphous PEK. The PEK-CNT composite was then equilibrated in NPT ensemble at 1 atm. (independent barostats in all 3 directions) to remove any empty space between CNT and the matrix. Afterwards, the composite structure was equilibrated using NVT and NVE to get final structure with final dimensions of 98.5Å×95.2Å×39.3Å. The procedure is shown in Fig. 1 schematically. The time step of 0.5 fs was chosen for all the MD simulations.

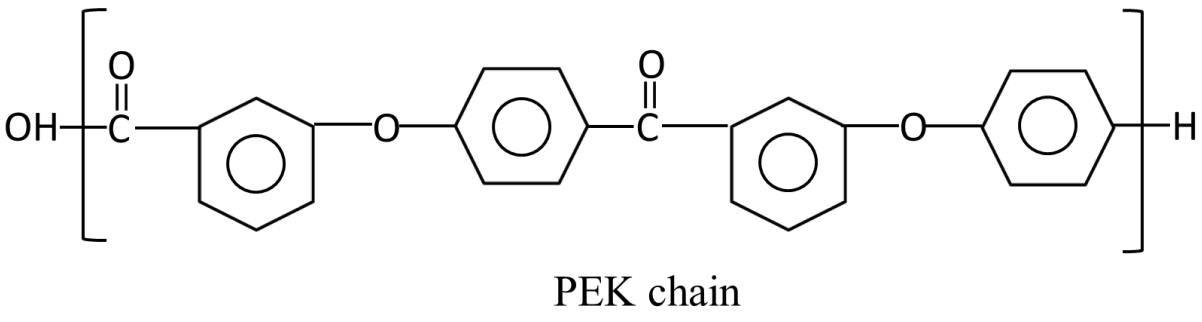

Figure 12: Schematic of single PEK chain

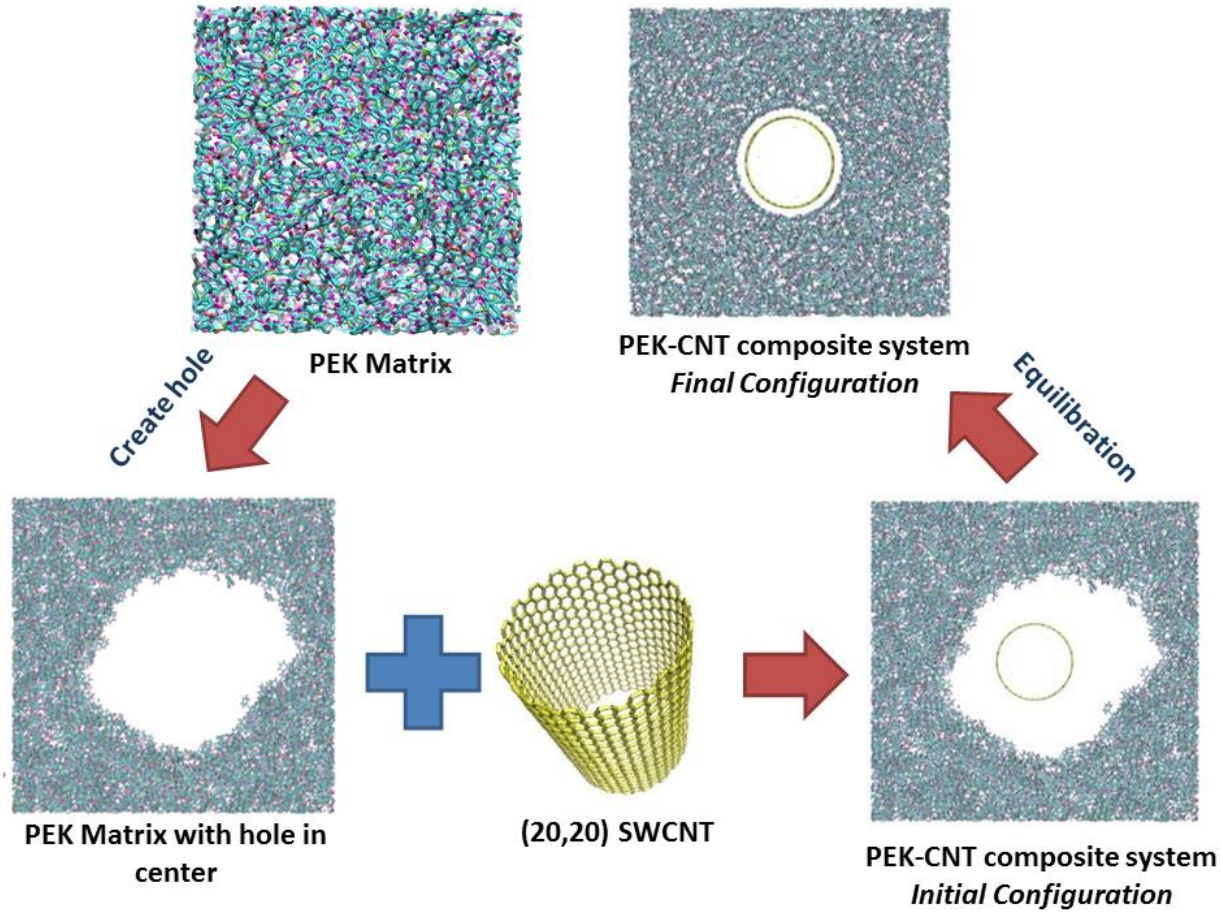

Figure 13: The procedure of creating CNT/PEK composite.

3.1.3 Create Crosslinked Functionalized CNT

In this study, the PEK oligomer ends are grafted on the CNT on the basis of Friedel Crafts acylation reaction, as observed in the experimental studies [33, 74, 75]. In this reaction, the carbon atom of the carboxylic acid group (-COOH) of PEK is covalently bonded to carbon atom of CNT (Fig. 2a) [75]. In order to functionalize CNT, we have followed the functionalization procedure as outlined in a recent study on graphitic functionalization [68].

Here, the PEK chains within a certain radial distance (≤ 5Å) to CNT are chosen as possible candidates for reaction within the equilibrated composite system. The carbonyl carbon is chosen as the first reactive site while the CNTs' carbon atom closest to carbonyl carbon of PEK is chosen as the second reactive site. As most of the carbonyl ends of the PEK chain are not within the distance ≤ 5Å of CNT surface, we drag these ends located outside this region (depending on the number of bonds to be formed) and bring them closer to CNT. In order to chemically activate the PEK chain, hydroxyl group (-OH) is removed from carboxylic acid group, and the carbon atom of carbonyl group (denoted as C_4, afterwards) is bonded to the CNT. To maintain the charge neutrality of the system, the charges are redistributed between activated carbon atoms of CNT and the carbonyl carbon atoms. The aforementioned procedure is repeated for every new bond created in the system. Six cases of functionalized CNT are considered: 1, 5, 10, 20, 40, and 80 crosslinks between CNT and PEK, resulting in functionalization degree up to 6.25%. As a new bond is created, the corresponding bond, angle, dihedral angle and improper angle coefficients are also created/updated. The energy of new composite topology is minimized. Then the resulting composite structure is equilibrated again for 400 ps NVT (300 K), 100 ps in NPT (1 atm; 300 K) and 100 ps in NVE ensembles.

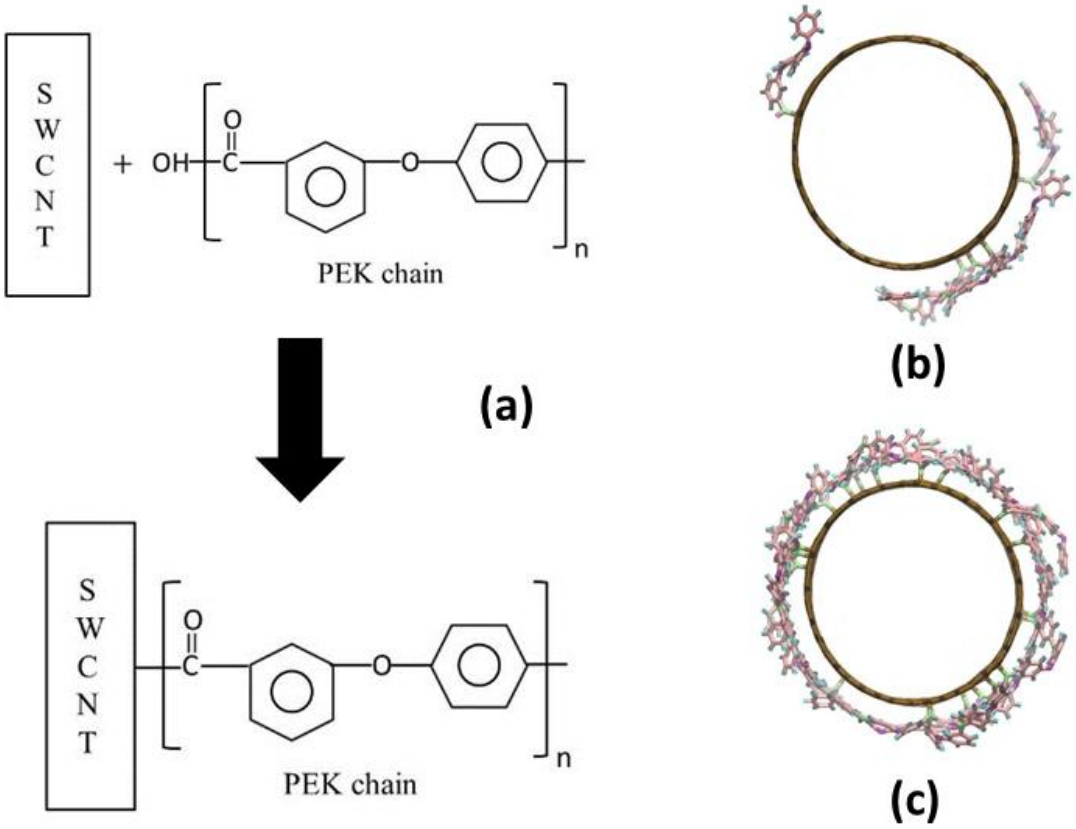

Figure 14: (a) Procedure of making covalent bond between CNT and a PEK chain; representative structure showing (b) 5-bonds and (c) 20 bonds between CNT and PEK

3.2 Computational Model for TBC

3.2.1 Thermal Boundary Conductance (TBC) by NEMD Methodology

After equilibration of non-functionalized and functionalized composite systems, thermal transport simulations are performed using NEMD methodology [47, 49, 53], in which a steady-state radial temperature gradient profile is generated under applied heat flux conditions. In order to obtain the temperature gradient profile of PEK matrix, it is divided into 8 concentric

cylindrical shells of thickness 7Å. To ensure that the temperature difference at the interface is large enough for TBC calculations, the heat rate Q=10.0e-8 W is applied to CNT. While heat rate Q is added to CNT, the energy is simultaneously subtracted at the same rate from the outmost layer of PEK matrix as shown in Fig. 3. For ensuring that system reaches steady-state in each case and temperature profile in cylindrical shells of PEK has reasonable statistical accuracy, 1 ns simulation is performed for each case. We choose last 600 ps data to calculate the average temperature of each cylindrical shell and generate the temperature profile. The temperature jump ΔT_j is the difference between the temperature of CNT and PEK at the interface, which is obtained by fitting solution of 1D-axisymetric heat conduction equation, i.e., $T = C_1 \ln(r) + C_2$.[49] Then, TBC (G) is calculated as[49, 67]

$$G = \frac{Q}{\Delta T_j A} \tag{2}$$

where A is the area of interface between CNT and PEK.

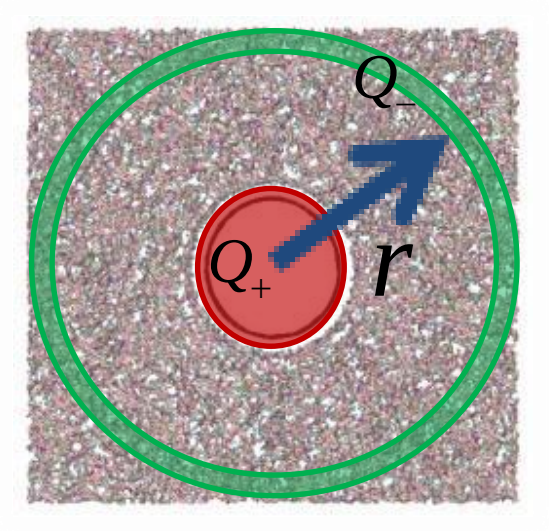

Figure 15: Schematic showing the cross-section of one of the studied systems (along *z*-axis). The red region encompasses CNT which is heated while the heat is removed from outmost layer of PEK matrix shown in green.

3.3 Spectral Analysis

3.3.1 Spectral Energy Density (SED) Methodology

Besides developing understanding of how the functionalized CNT influence the TBC, the detailed phonon energy distribution in CNT and interfacial phonon interactions between CNT and PEK matrix are also investigated in the present work. The analysis of phonon energy distribution in CNT is accomplished by the spectral energy density (SED) which is computed by taking 2D Fourier transform of the velocities of CNT atoms sampled in NVE ensemble for a period of 500 ps.[50, 65, 66, 85, 86] The Fourier transform for SED is taken with respect to wave vector k and frequency ω using following equation

$$\theta(\omega,k)=\frac{m}{2}\sum_{j}^{p}\sum_{\alpha}^{3}\left|\frac{1}{N}\sum_{n=0}^{N-1}\exp(ik_z z)\int v_{j,\alpha}(n,t)\exp(-i\omega t)dt\right|^2 \quad (3)$$

The SED is derived by projecting the positions of the CNT atoms onto vibrational normal modes. In Eqn. 2, m is the mass of a C atom of CNT, and k_z is the dimensionless wave vector ($k_z = 2\pi n / a_z N$) along z direction (axial direction). p is the number of atoms in the n^{th} unit cell and α represents the index of coordinate dimension. The SED is also used to calculate dispersion relation of the CNT.

3.3.2 Spectral Temperature Analysis

In order to analyze the thermal interactions between CNT and PEK, the CNT is subjected to pulsed heating followed by relaxation to room temperature. Here, CNT is first heated at 600K for 40ps while keeping PEK matrix at 300K. Then, the CNT and PEK matrix composite system is relaxed for 500ps in NVE. The frequency dependent energy distribution *g(ω)* during this process is calculated by Fourier transform of velocities of atoms as follows[50, 85] :

$$\mathrm{g}(\omega)=\frac{1}{3N_a}\sum_{j}^{p}\sum_{\alpha}^{3}\left|\sum_{n=0}^{N-1}\int v_{j,\alpha}(n,t)\exp(-i\omega t)dt\right|^2 \quad (4)$$

At equilibrium, the energy is assumed to evenly distributed in all the modes of CNT. The equilibrium spectrum energy, $g_{eq}(\omega)$, can then be defined as

$$g_{eq}(\omega)=\rho(\omega)k_B T_{eq} \quad (5)$$

where $\rho(\omega)$ is the phonon density of states and T_{eq} is the equilibrium temperature. The phonon density of states can be written as

$$\rho(\omega) = \frac{g_{eq}(\omega)}{k_B T_{eq}} \tag{6}$$

However, once CNT is heated, the equilibrium state of vibrational modes is disturbed and the phonon energy distribution of CNT depends on the phonon scattering to different modes and thermal transport to the surrounding matrix. The spectral temperature $T_{sp}(\omega,t)$ of CNT in different non-functionalized/functionalized cases measures the energy distribution in different frequency bands with time. The expression for the transient energy distribution, g_{neq}, can be written as:

$$g_{neq}(\omega,t) = \rho(\omega) k_B T_{sp}(\omega,t) \tag{7}$$

In order to obtain the transient energy spectrum, the Fourier transform of velocity profiles is used similar to SED calculations. The sampling rate used for Fourier transform is 200THz, which corresponds to the 5fs interval between data points obtained from the MD simulation. Spectral temperature can be derived as

$$T_{sp}(\omega,t) = \frac{g_{neq}(\omega,t)}{g_{eq}(\omega)} T_{eq} \tag{8}$$

For this study, the frequency bands for the spectral temperature calculation are decided by observing the overlap between power spectrum of CNT and PEK matrix in equilibrium state and to avoid peaks in power spectrum at the boundary between two bands. The power spectrum is calculated for aromatic carbon atoms of PEK (C_1), the carbon atoms and oxygen atoms of carbonyl group (C_4 and O_1), and oxygen atoms of hydroxyl group (O_2) of PEK, in addition to

carbon atoms of CNT. The identified frequency bands as shown in Figure 4 are: 0-9 THz, 9-20 THz, 20-40 THz, and 40-68 THz.

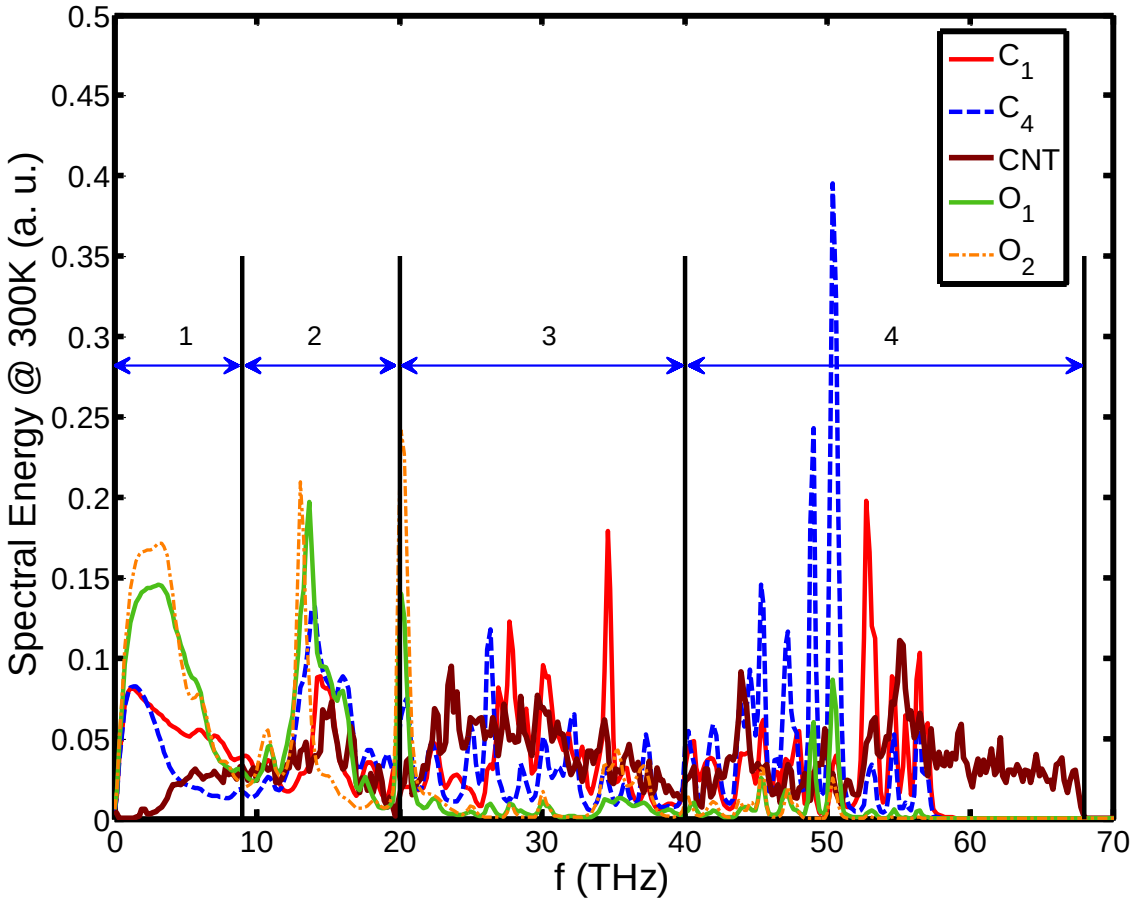

Figure 16: Power spectra of carbon atoms of CNT and specific atoms of PEK: aromatic carbon (C_1), the carbon and oxygen atoms of carbonyl group (C_4 and O_1), and oxygen atoms of hydroxyl group (O_2).

Eventually, the spectral temperature of SWCNT at different time for each band can be determined as follows:

$$T_{sp}(t) = \frac{T_{eq}}{\omega_1 - \omega_2} \int_{\omega_1}^{\omega_2} \frac{g^{neq}(\omega)}{g^{eq}(\omega)} d\omega \tag{9}$$

where ω_1 is lower limit and ω_2 is the upper limit of the frequency band.

CHAPTER 4

RESULTS AND ANALYSIS

The results and analysis presented in Chapter 4 are divided into two main Sections. The 1st Section, 4.1, presents thermal boundary conductance (TBC) between PEK and CNT and elucidate how the number of crosslinks bonded on CNT affect the TBC and interfacial thermal transport. The 2nd section, 4.2, summarizes and explains the results based on the spectral analysis. First, phonon dispersion curves of isolated and embedded CNTs estimated by SED are shown. Second, interfacial energy transfer in different frequency bands are discussed. The frequency regime is divided into 4 bands based on the overlapping of spectra and the spectral temperature calculations of these frequency bands for both non-bonded and bonded cases (~ CNT cross-linked with PEK) are discussed to decipher which band is the most efficient for energy transfer and how it is affected by increasing the number of cross-links between CNT and PEK. Third, to understand how the atoms in crosslinks participate in energy exchange, CNTs are heated using short temperature pulses and then relaxed, and the instant spectra at different time instants and relaxation time of different frequency bands are analyzed. Finally, comparisons with previous results in the literature are performed and findings are summarized.

4.1 Thermal Boundary Conductance (TBC) based on NEMD method

The thermal boundary conductance (TBC) at the interface of non-functionalized/ functionalized nanostructured materials and substrate was performed using two different methods in previous studies [1, 11, 12, 47, 53, 68, 87-90]. The first one is lumped capacitance methodology, which assumed the thermal resistance of intra-SWCNT will be much smaller than the thermal resistance at the interface between SWCNT and surrounding matrix. Maruyama S., *et*

al. used a bundle of CNTs (7 CNTs) to calculate the inter-tube TBC by fixing the temperature 300K for surrounding CNTs and 400K for central CNT [91]. After 10ps, the central CNT is relaxed and temperature difference between central CNT and surrounding CNTs is calculated. The temperature profile can be fitted to an exponential function. Compared with intra-tube resistance, the inter-tube resistance is larger to impede heat transfer. The Biot number calculated based on the characteristic length and thermal conductivity of central CNT suggests that the lumped capacitance method is applicable for calculating TBC between central CNT and surrounding material with larger heat capacitance and volume. Similar simulation was performed for SWCNT with surrounding water liquid matrix.[11]

S. Hida *et al*.[49] and Rajabpour *et al.* [92] derived the interface thermal boundary conductance (TBC) based on temperature decay history. In the study by S. Hida *et al*.[49], (10, 10) SWCNT was heated to a high temperature while surrounding matrix was fixed at lower temperature compared to the temperature of SWCNT. After SWCNT thermostat was released, the temperature decay history of SWCNT was modeled as exponential decay $\Delta T = \Delta T_o e^{-t/\tau_T}$, where ΔT_o was the original temperature difference between temperature of SWCNT, $T_{CNT,o}$, and the temperature of substrate, $T_{\text{sub},o}$, at the beginning of the relaxation period and τ_T is the relaxation time for the temperature decay. Following energy conservation in both bodies:

$$\frac{\partial T_{CNT}}{\partial t} = -\frac{1}{k_B N_{CNT}} G^t \Delta T \tag{10}$$

and

$$\frac{\partial T_{sub}}{\partial t} = -\frac{1}{k_B N_{sub}} G^t \Delta T \tag{11}$$

Here $G^t = GA$ and finally, the TBC was calculated using Eqn. (12) [92]:

$$G = \frac{k_B}{\tau_T A} \cdot \frac{N_{CNT} N_{sub}}{N_{CNT} + N_{sub}} \tag{12}$$

where k_B is the Boltzmann constant and N is the number of degrees of freedom for SWCNT or surrounding matrix, and A is the interfacial contact area respectively.

Shenogin *et al*. [12] applied both lumped capacitance method and NEMD method for TBC. The difference between two methods was about 30%. In this study, we tried to use both methods to calculate TBC for different functionalized cases. However, we found that the difference of results between lumped capacitance method and NEMD method increases significantly (> 100 %) as the number of crosslinks bonded with CNT increased. The primary assumption for lumped capacitance method was that the intra-tube resistance of CNT should be much smaller than the resistance at the interface [91]. However, while crosslinks were bonded with CNT, the defects on CNT were created and they would scatter phonon along surface of CNT. This might increase the intra-tube resistance of CNT as the thermal conductivity of CNT also decreased [68]. Accuracy of lumped capacitance method has been questioned in literature before [92]. Considering the large difference between lumped capacitance method and NEMD method for the cases of functionalized CNT, we only use NEMD method for the rest of discussion followed.

In order to analyze the effect of functionalization on thermal transport at CNT-PEK interface, TBC was calculated for seven cases: no crosslinks (0%), 1 crosslink (0.08%), 5 crosslinks (0.39%), 10 crosslinks (0.78%), 20 crosslinks (1.56%), 40 crosslinks (3.12%) and 80 crosslinks (6.25%), using NEMD method following Eqn. 1. In this context, the steady-state

temperature profiles for unfunctionalized and different functionalized cases as a function of radial distance from CNT are shown in Fig. 5. For the case of non-functionalized CNT, largest temperature discontinuity at the interface is observed, which keeps decreasing as the number of crosslinks increase. The observed decrease is indicative of more thermal energy transport channels between CNT and PEK matrix as number of covalent bonds increase. The results of TBC calculated by Eqn. 1 are shown in inset of Fig. 5 revealing how degree of covalent functionalization increases TBC.

The previous experimental and simulation studies [11, 47, 53, 54, 93] report TBC of non-functionalized CNT embedded in polymer matrix on the order of ~ 100 MW/m^2-K (thermal boundary resistance ~ 10^{-8} m^2-K/W). In our simulations, the calculated TBC is observed to be 23.58 MW/m^2-K for the CNT/PEK interface without any covalent bonding, which is in agreement with the previously studies for non-bonded interfaces [11, 47, 53, 54, 93]. In addition, similar to previous literature [47, 54], we also observe a linear increase in TBC with number of cross-links or degree of functionalization.

In the experiments by Jain *et al.* to fabricate fibers from CNT and PEK matrix, only 3% functionalization of CNT (3 atom per 100 atoms of CNT) could be achieved [13, 33], hence we limited our study to only up to 6.25% functionalization at which largest TBC of 236.44 MW/m^2-K was observed. A 5-fold and an order of magnitude increase in TBC for 3.12% and 6.25% functionalization, respectively, compared to non-functionalized case is very promising for CNT-PEK composites or fibers. Overall, the functionalization results in the stronger thermal coupling between sidewall CNT and PEK matrix, leading to higher values of TBC.

It is well known that functionalization creates defects on CNT surface, which increase phonon scattering and impede phonon propagation along the CNT axis, decreasing its intrinsic thermal conductivity. So, the effective thermal conductivity of fibers or nano-composites made by CNT/PEK is a result of interplay between the two competing factors, i.e., increase in TBC and decrease in thermal conductivity of the fillers such as CNTs. Kuang *et al*.[48] and S. Hida *et al*.[49] calculated the thermal conductivity of polymer composite based on effective medium model[94] and show significant increase in the effective conductivity of composite irrespective of decrease in CNT conductivity. In the experiments by Jain *et al.*, a large increase in effective thermal conductivity of PEK grafted CNT fiber was observed as well [33]. Such observations confirm that the increase in TBC due to filler functionalization is an important reason for high increase in thermal conductivity of polymeric nanocomposites, and hence, is a vital parameter to be analyzed in greater detail.

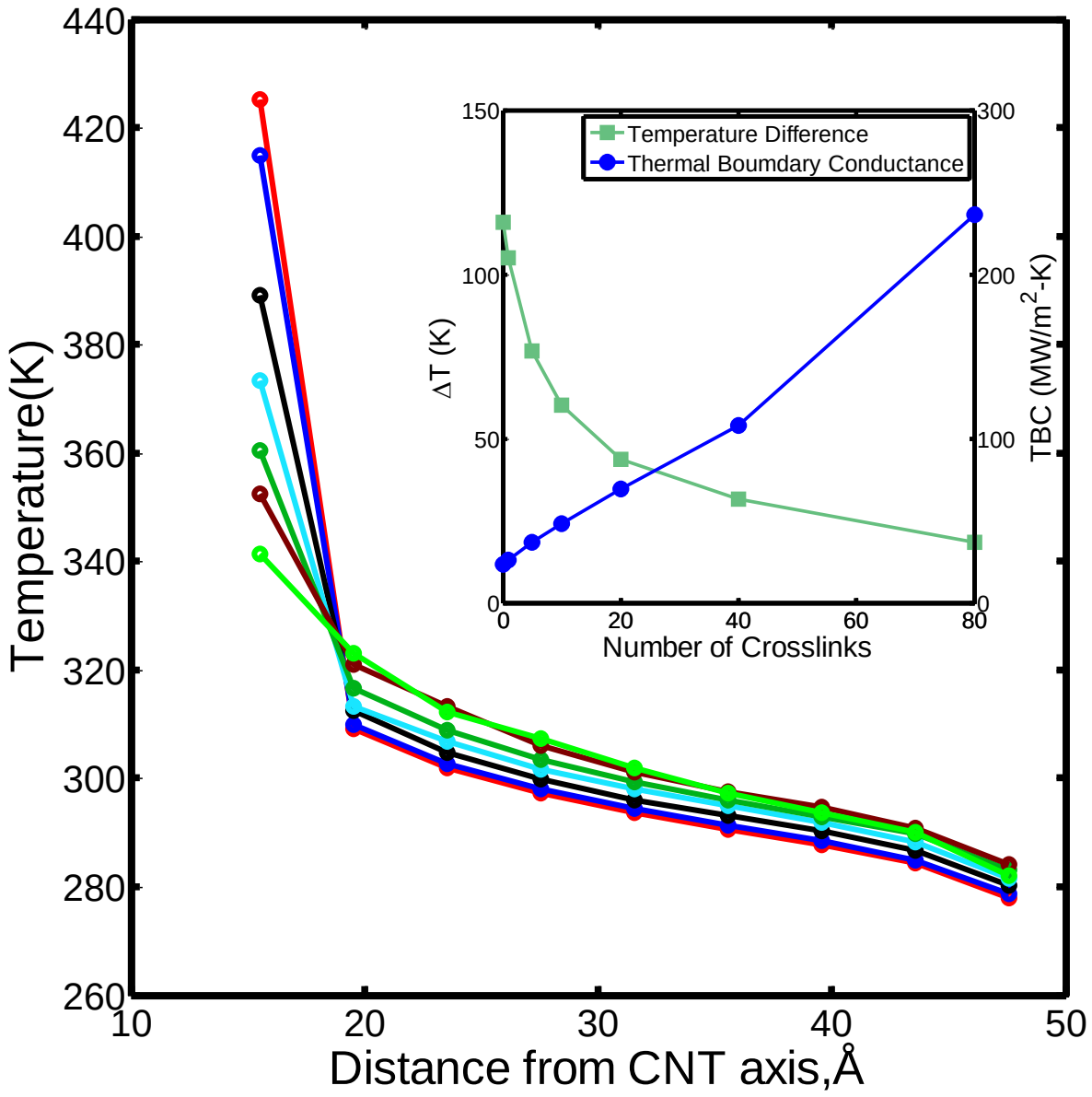

Figure 17: Radial distribution of system temperature under steady-state for 7 studied cases: no crosslinks (red) (0%), 1 crosslink (blue) (0.08%), 5 crosslinks (black) (0.39%), 10 crosslinks (cyan) (0.78%), 20 crosslinks (dark green) (1.56%), 40 crosslinks (brown) (3.12%) and 80 crosslinks (green) (6.25%). The inset shows the temperature difference and thermal boundary conductance at the interface of CNT-PEK for different cases.

4.2 Spectral Analysis

4.2.1 SED analysis for (20,20) SWCNT

The SED calculations provide detailed comparison of phonon dispersion relations between isolated and embedded CNT. 2D phonon energy spectrum for isolated and embedded (20, 20) CNT is computed using spectral energy density (SED) method (Eqn. 3). Fig. 18a & 18b present the SED contour plots as a function of frequency (*f*) and wave vector (*k*), which is also referred to as phonon dispersion relationship. In Figure 18, k^* is the dimensionless wave vector which is non-dimensionalized by $2\pi / a_z$, where a_z is lattice constant along CNT axial direction [85, 86]. SED is averaged over all CNT atoms and the discreteness in dispersion curve is due to the finite size of the CNT in the simulation. Comparing the phonon dispersion relation of isolated CNT with that of embedded CNT, it can be observed that the dispersion is similar except in the low frequency region, 0-9 THz (red box in Fig. 18a & 18b). In this region, the dispersion branches of the embedded CNT are diffused due to phonon scattering by PEK,[50] suggesting that the low frequency phonon modes of CNT damps strongly in presence of the surrounding matrix. The dispersion relation above 40THz, corresponding to optical modes, is notably altered for embedded CNTs, i.e., higher frequency in LO mode can be observed for embedded CNT and is attributed to the slight deformation of embedded CNT. The van der Waals interaction between CNT and polymer matrix alters the original structure of CNT, which in turn, modifies the dispersion of optical modes for embedded CNT.

In order to understand how the covalent functionalization modify the phonon energy distribution of CNT, energy spectra following Eqn. 4 is also calculated for isolated, embedded, 10-bonded, 40-bonded, and 80-bonded CNT cases at room temperature. As shown in Fig. 19, for

low frequency band (0-9THz), the normalized power spectrum of isolated CNT has more energy peaks than the other cases. The spectrum of embedded CNT is suppressed especially at low frequencies due to CNT-PEK van der Waals (vdW) interactions. Comparing low frequency band spectra in black dashed box in Fig. 19, it can be observed that as the number of covalent bonds increases, the peaks of energy spectrum suppressed more significantly and the entire low frequency spectrum become smoother. This is related to previous analysis that the crosslinks provided channels for interfacial thermal transport and covalent functionalization enhances the efficiency of energy transfer. The covalent bonds between PEK and CNT assists the energy transfer along the crosslinks into the polymer matrix, which strengthens thermal coupling at the interface leading to high thermal boundary conductance. This suppression of energy peaks has also been previously observed in the multi-walled CNT (MWCNT) with polyethylene crosslinks and single-walled (SWCNT) in solid and liquid argon matrices [48, 50]. Compared to low frequency band, the suppression for rest of the frequency bands is weaker for all functionalized cases as there are relatively less overlap between the spectra of intermediate and high frequency bands of CNT and PEK matrix. In high frequency band (40-68THz), the energy peaks for embedded and functionalized CNT shifts to slightly higher frequencies due to interaction with PEK (Fig. 19). However, with increasing number of bonds, the energy distribution and location of peaks in high frequency region does not change appreciably.

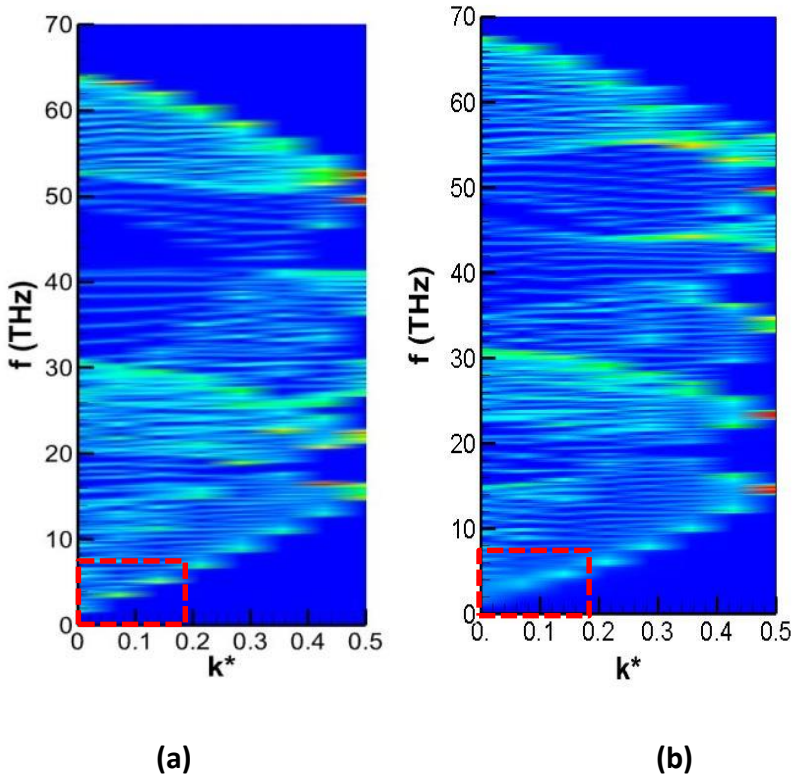

Figure 18: Phonon dispersion relation for (a) isolated CNT; and (b) embedded CNT computed using SED.

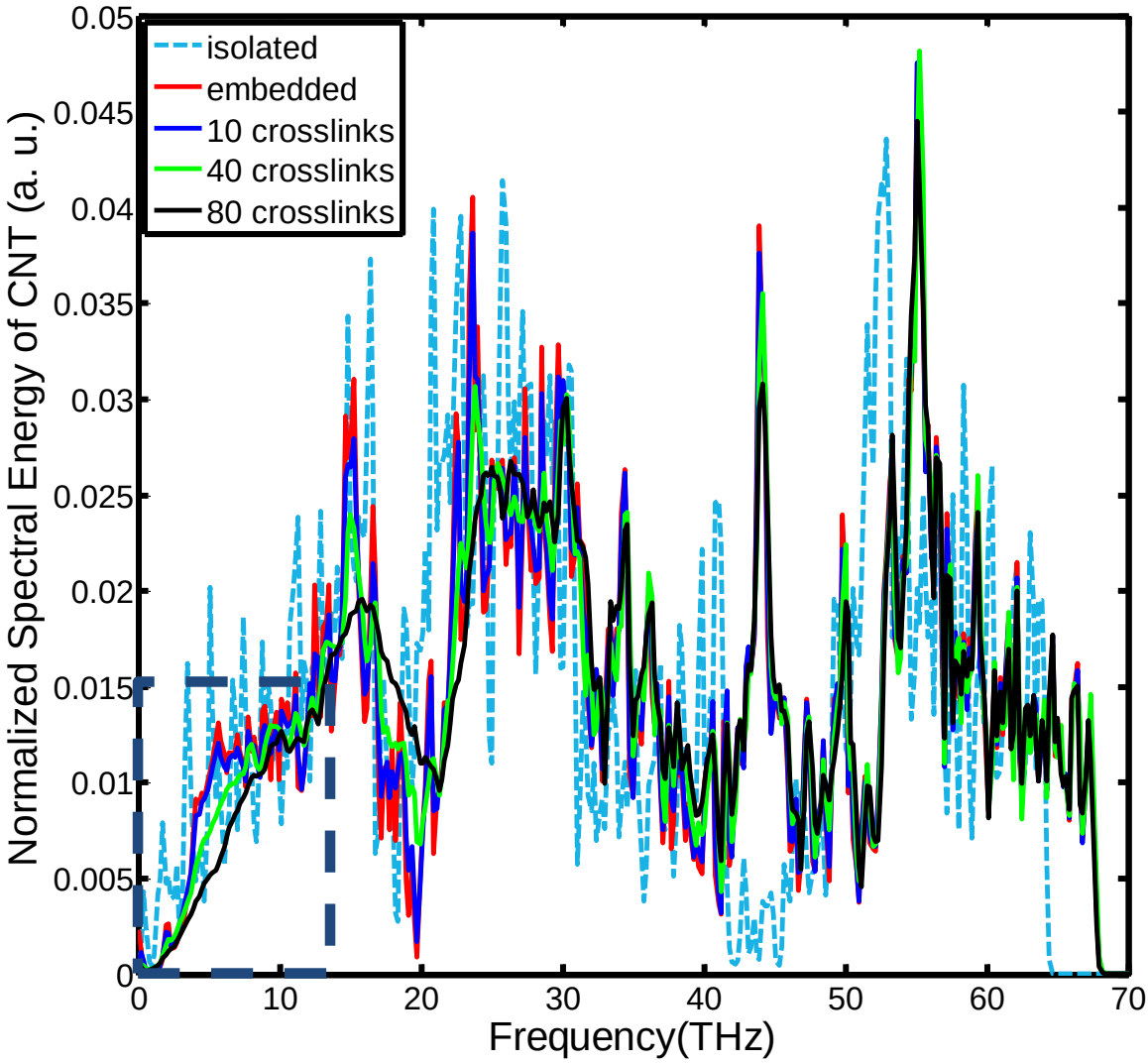

Figure 19: Normalized spectral energy for CNT for isolated, embedded, 10 crosslinks, 40 crosslinks and 80 crosslinks cases.

By analyzing normalized power spectra of CNTs among all cases at room temperature, it is evident that the covalent functionalization has notable effect on the energy distribution. In addition to frequency domain, it is interesting to investigate how the energies of different phonons are affected in time domain as the heat energy is transferred from CNT to PEK matrix. In this context, the non-functionalized CNT is first heated at 600K for 40 ps and subsequently

relaxed to reach in equilibrium with surrounding matrix. The transient power spectrum of CNT following Eqn. 7 is computed to decipher energy distribution change with time for different frequencies. The cases of non-functionalized embedded CNT, 10 crosslinks CNT, 40 crosslinks CNT and 80 crosslinks CNT are chosen for the discussion here and are shown in Fig. 20. It is shown that the energy peaks are higher at the beginning of simulation due to the heating at high temperature but decay quickly within 100ps. Compared to the transient spectrum of unfunctionalized CNT, the 40 crosslinks CNT spectrum decay relatively faster. In addition, the energy decay for functionalized case for both high and low energy peaks is faster due to efficient thermal transport enabled by the crosslinks with PEK matrix.

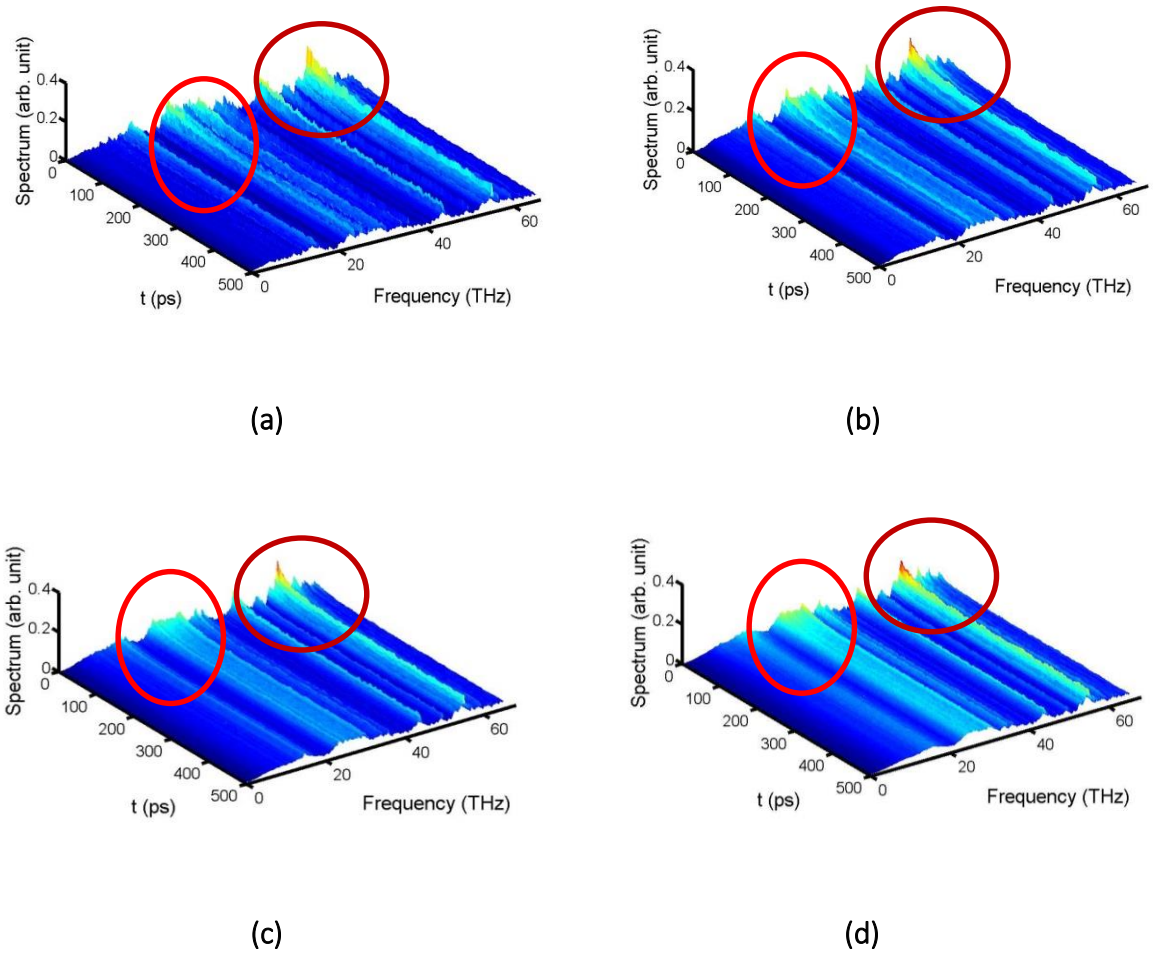

Figure 20: Transient spectra for (a) no crosslinks CNT, (b) 10 crosslinks CNT, (c) 40 crosslinks CNT and (d) 80 crosslinks CNT.

4.2.2 Transient Spectrum and Equilibrium Spectrum Analysis for (20, 20) SWCNT & Atoms of Crosslinks

Since the crosslink plays a major role to influence interfacial TBC, it is necessary to comprehend how different types of atoms in crosslink change the process of heat dissipation in various frequency bands. We perform spectral energy analysis of selected cross-link atoms to

elucidate the thermal energy transfer from CNT to PEK for both non-functionalized and functionalized cases. We calculated the transient spectra of aromatic carbon C_1, and carbonyl carbon C_4 and oxygen O_1 atoms (see the Fig. 21) for non-bonded, 40-bonded and 80-bonded cases.

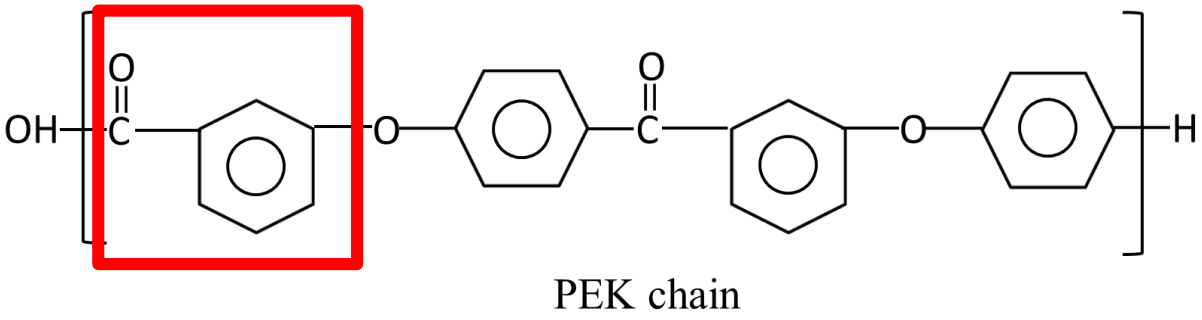

Figure 21: The atoms indicated in red box are C_1 (benzene ring carbon atoms), C_4 (carbon atom of carboxyl), O_1 (oxygen atom of carboxyl) in crosslinks for spectra analysis.

At first, transient spectra of atoms of 10 crosslinks and the same atoms in no crosslinks case are presented. Fig. 22a & 22b present spectra for atoms C_1 in PEK chains. The spectrum of C_1 in the no crosslinks case has more peaks than the spectrum of the 10 crosslinks case, especially in the low frequency regime. Above the low frequency regime, the energy peaks of the no crosslinks case change slowly with time. Inversely, the energy peaks at the similar frequency domain for the 10 crosslinks case are higher at the beginning due to the high energy transfer from CNT, but those peaks decay quickly and then maintain similar power strength for the rest of simulation time (see Fig. 22). The following Figure 23 shows the spectra of C_4 for 0 crosslinks- case and of the same atoms in no crosslinks case. Likewise, the spectrum of C_4 of the bonded case is smoother at the low frequency regime; the high frequency peak around 50 THz has the highest energy at the beginning. Based on the spectra, it can be mentioned that different

atoms of crosslinks may interact with CNT in different frequency regimes. C_1 and C_4 atoms correspond to the energy transfer at mid and high frequency regimes. The spectra of 10 crosslinks O_1 (Fig. 24) reveal that O_1 atoms have more high energy peaks at the low frequency regime than C_1 and C_4 atoms in crosslinks. Although the energy peak at mid frequency disappears in O_1 spectrum for the crosslink case, low frequency peaks are more intense compared with the non-crosslink case. Overall, this observation indicates that the crosslinks bonded with CNT help in the efficient energy transfer in both low and high frequency regimes. We will have more detailed discussions about the comparisons of energy decay in different frequency regimes among different crosslinks cases in the following sections (also see Appendix C). As the spectrum do not change much after 250 ps, we just focus the analysis on different time instants less than 250 ps when comparing different crosslinks cases.

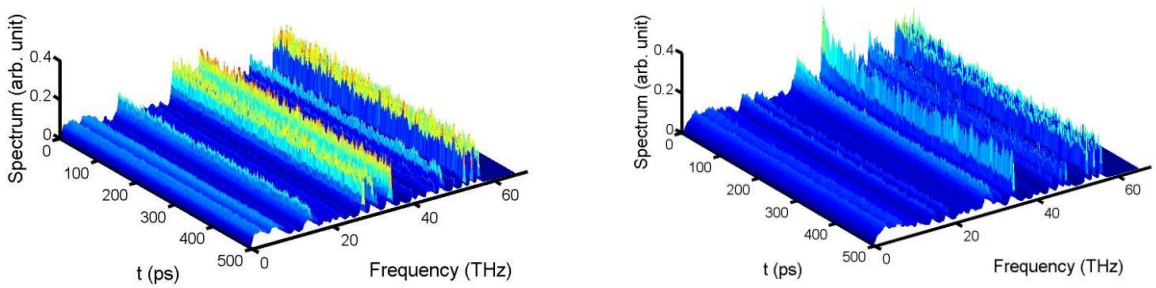

(a) (b)

Figure 22: The transient spectra of aromatic carbon atoms (C_1) in same polymer chains of (a) no crosslinks and (b) 10 crosslinks cases

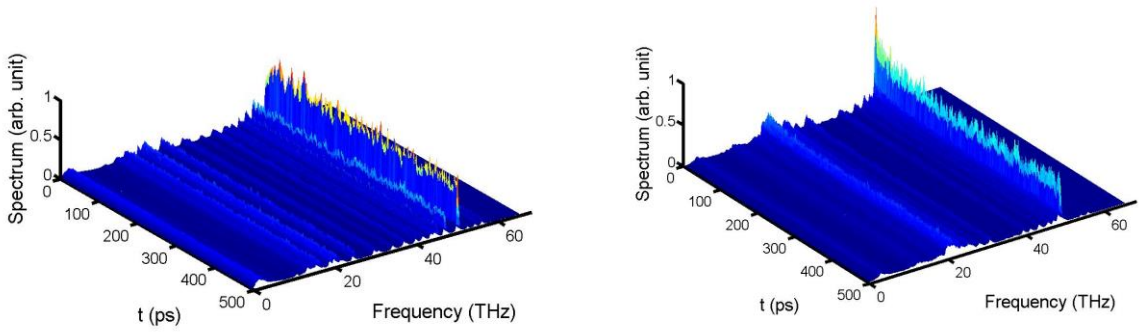

(a) (b)

Figure 23: The transient spectra of carboxyl carbon atoms (C_4) in same polymer chains of (a) no crosslinks and (b) 10 crosslinks cases

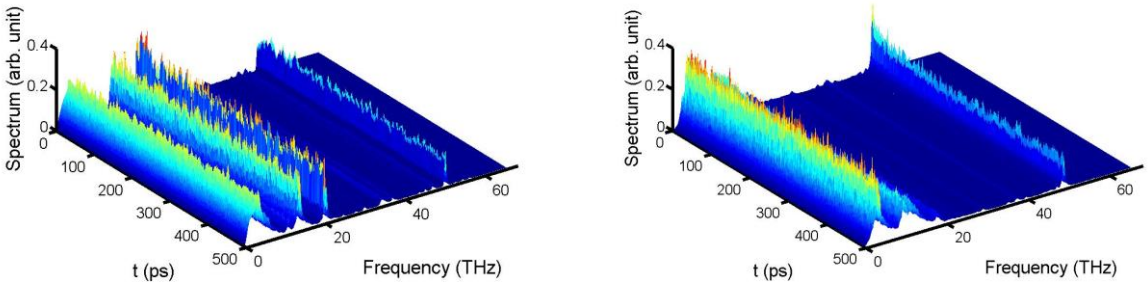

(a) (b)

Figure 24: The transient spectra of carboxyl oxygen atoms (O_1) in same polymer chains of (a) non-bonded and (b) 10 crosslinks case.

Change of power spectra with time reveal the effect of covalent functionalization on energy transfer between CNT and PEK matrix. Since the crosslinks play a major role in

interfacial thermal transport, it is necessary to comprehend the process of energy transfer with increasing number of cross-links using the spectral energy analysis of atoms which are either involved or are in the vicinity of the crosslinks. Power spectra of C_1 (aromatic carbon atoms), C_4, and O_1 (carbon & oxygen atoms of carbonyl group in PEK) are calculated for non-functionalized, 40 crosslinks and 80 crosslinks cases at 0ps, 50ps, 80ps, and 100ps from the beginning of thermal relaxation of the CNT (t=0 ps) heated at 600K.

As mentioned previously in Chapter 3, the frequency domain is divided into 4 regimes based on frequency bands overlapping between CNT and atoms of PEK, low frequency region (0-9THz), mid frequency regions (9-20THz and 20-40THz), and high frequency region (40-68THz). The spectra show how the energy decays in different frequency regimes at different time; no-crosslink cases and crosslink cases are compared with each other. Fig. 26 compares the transient spectral energy decay between no crosslink case and one of the crosslinks cases (40 crosslinks case) for different PEK atomic entities at different stage of thermal energy relaxation. At the beginning of relaxation process (t=0 ps), the aromatic carbon atoms, C_1, of bonded crosslinks have higher energy in the 1^{st} frequency (0-9 THz) and 2^{nd} frequency bands (9-20 THz) than the same C_1 atoms in the no-crosslink case (Fig. 32a). Plots show that C_1 atoms have similar magnitude of energy peaks in high frequency band at 0ps (Fig. 26a). At 50ps and 100ps (Fig. 26b-c), the energy peaks of 2^{nd}, 3^{rd} and 4^{th} bands are smaller for 40 crosslinks case than those of no crosslinks case, which suggests that phonon energy decay of 2^{nd}, 3^{rd} and 4^{th} bands for C_1 in 40 crosslinks is much faster than that of no crosslinks case. This suggests that C_1 atoms in bonded crosslinks significantly assist in energy transfer in 2^{nd}, 3^{rd} and 4^{th} frequency bands from CNT to PEK matrix. It is also worth noting that the low frequency band spectra of C_1 in bonded

crosslinks are smoother and the overlapping area is larger compared to those of C_1 in non-bonded crosslinks.

Considering transient power spectrum of C atom of carbonyl group, C_4, the most effective energy decay is in the 4th band, which is around 40-50THz (see Fig. 26d-f). Since the energy peaks in spectra of C_4 in low frequency band is very small in magnitude, C_4 atoms of crosslinks in both non-bonded and bonded cases are not efficient in energy transfer in low frequency region. The oxygen atom of carbonyl group, O_1, of both non-bonded/bonded cases mainly contribute to energy decay in low frequency band (see Fig. 26g-i) as most of the peaks of energy spectrum for O_1 are located in 0-20THz. After functionalization of CNT, spectra of O_1 atoms broaden in 0-20THz region and the energy decay is faster in this region compared to no cross-link case, which further suggests that O_1 atoms are important for energy transfer in low frequency region. In summary, the atoms of crosslinks bonded with CNT have smoother and broader spectra after functionalization. The spectra of functionalized CNTs are smoothened but suppressed, and spectra of atoms in bonded crosslinks are smoothened and broadened.

On noticing that there is significant modification in spectra of crosslinks in non-bonded and bonded cases, we plotted and compared similar spectra for PEK atoms (C_1, C_4, O_1) with different degree of CNT functionalization (10, 40 and 80 crosslinks) for 3 different time instants, (0 ps, 50 ps, and 100 ps), which is shown in Fig. 28. The changes in transient power spectra of different types of atoms in crosslinks for different degree of functionalization should help in deciphering mechanism of thermal transport with increasing number of covalent bonds. The spectra for 10 crosslinks case and 80 crosslinks case at three different time instants (0 ps, 50 ps, and 100 ps) is also shown separately in Fig. 25 and Fig. 27, respectively. The spectra presented in these figures are integrated over all atoms in crosslinks in each case. The spectra of 80-bonded

case have highest peaks for C_1, C_4 and O_1, i.e., for 80-bonded case atoms in PEK absorb more energy than other cases. The power spectra of carbonyl oxygen atoms (O_1) in crosslinks suggest that the energy transfer to these atoms from CNT is dominant in low frequency region (0-20 THz) (Fig. 28g-i). Compared with O_1 atoms, C_1 atoms contribute to energy transfer in entire frequency domain including mid-frequency and high-frequency region (Fig. 28a-c). C_4 atoms contribute energy transfer in mid- and high-frequency region but do not contribute much at low frequency region in all cases (Fig.28d-f).

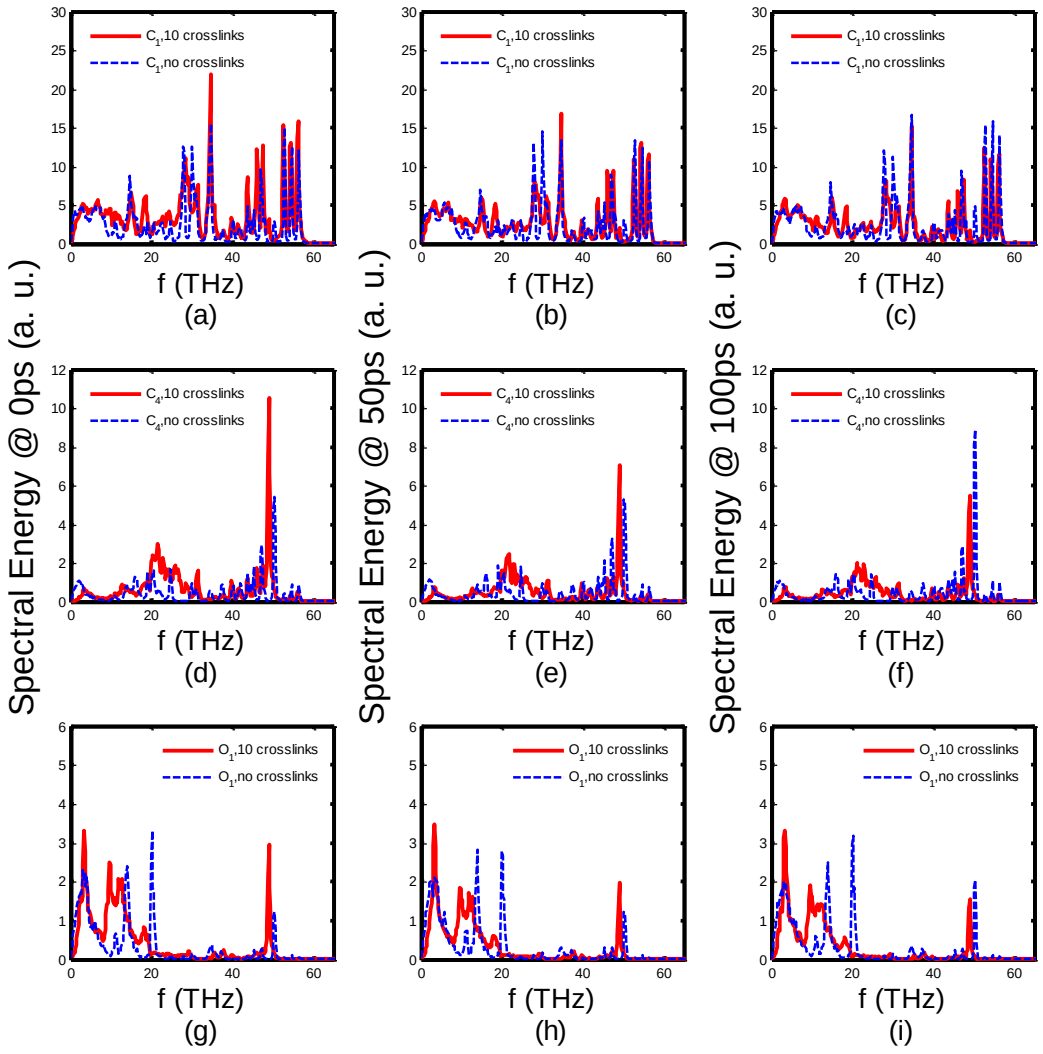

Figure 25: The power spectra of aromatic carbon atoms (C_1), carboxyl carbon atoms (C_4), carboxyl oxygen atoms (O_1) in same polymer chains of no crosslinks and 10 crosslinks cases at 0ps, 50ps and 100ps.

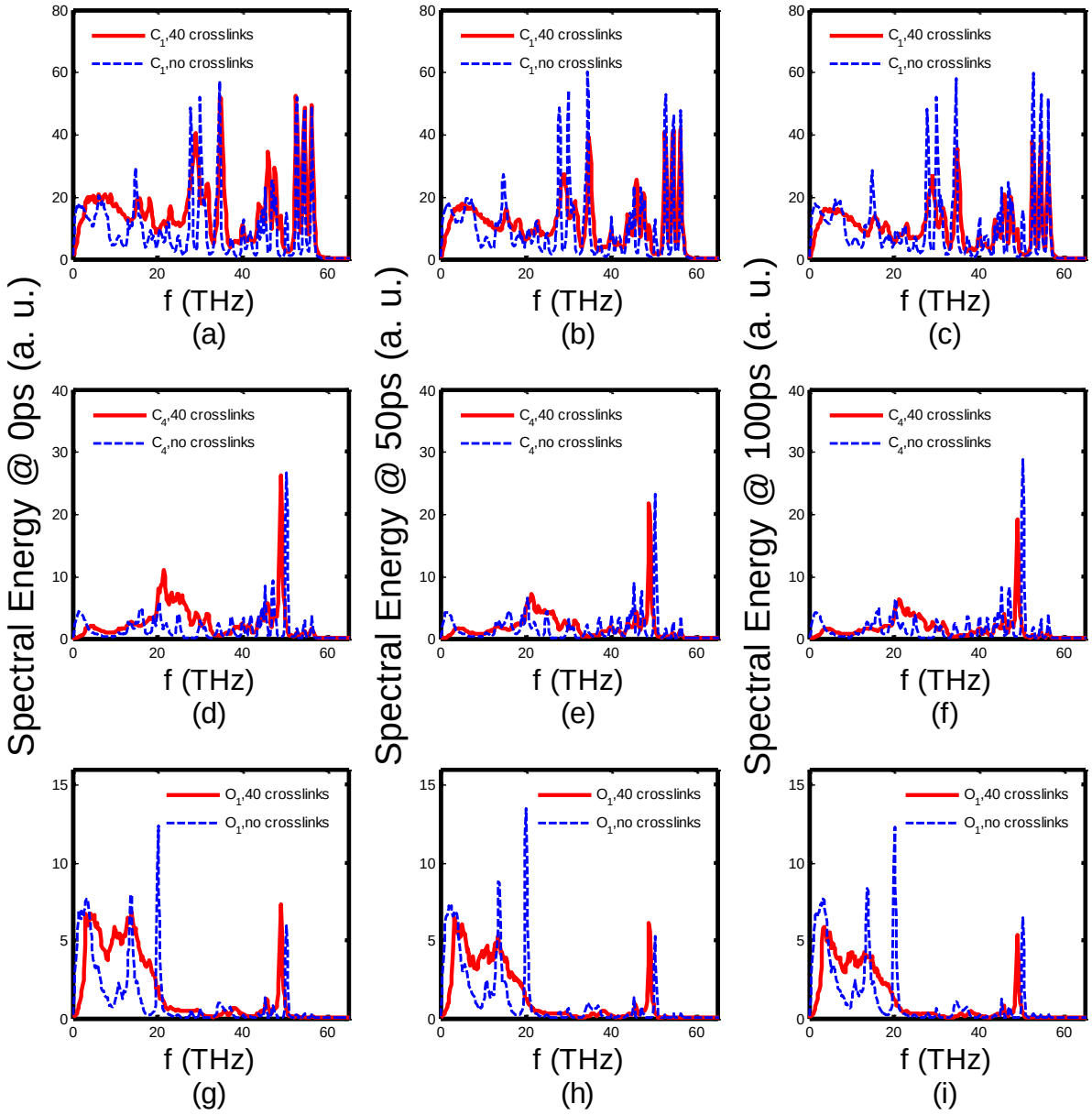

Figure 26: The power spectra of aromatic carbon atoms (C_1), carboxyl carbon atoms (C_4), carboxyl oxygen atoms (O_1) in same polymer chains of no crosslinks and 40 crosslinks cases at 0ps, 50ps and 100ps.

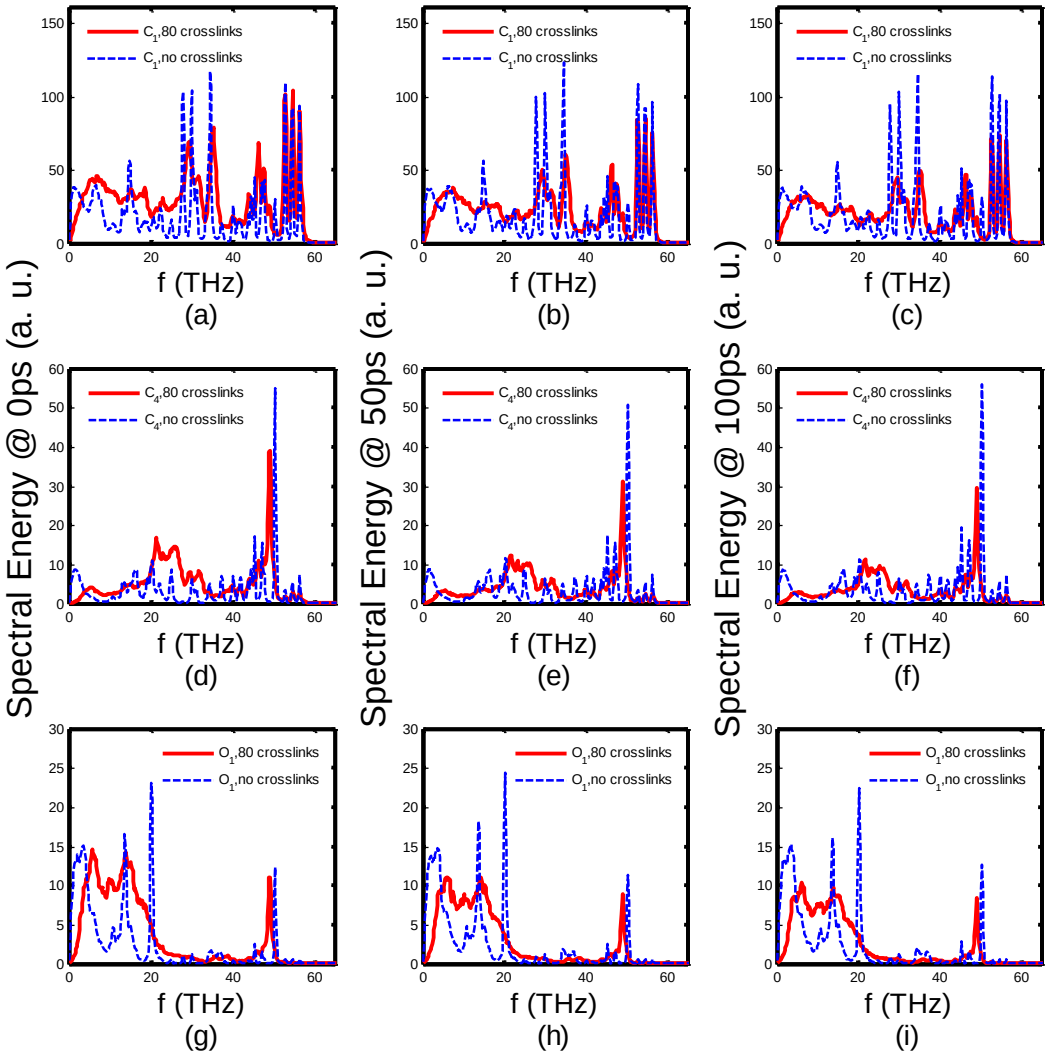

Figure 27: The power spectra of aromatic carbon atoms (C_1), carboxyl carbon atoms (C_4), carboxyl oxygen atoms (O_1) in same polymer chains of no crosslinks and 80 crosslinks cases at 0ps, 50ps and 100ps.

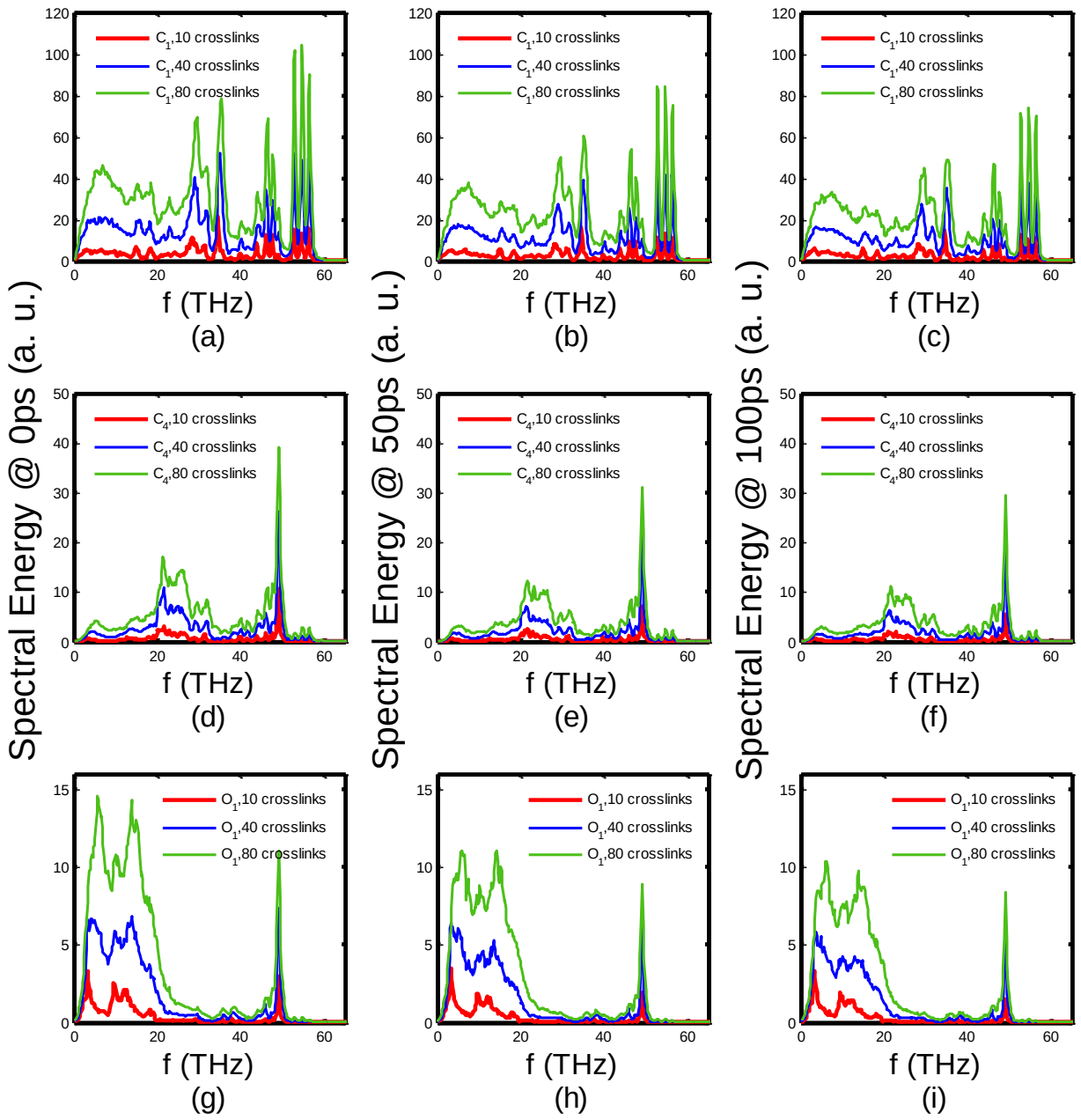

Figure 28: The power spectra of aromatic carbon atoms (C_1), carboxyl carbon atoms (C_4), carboxyl oxygen atoms (O_1) of 10 crosslinks, 40 crosslinks and 80 crosslinks cases at 0ps, 50ps and 100ps.

Previous studies suggested that compared to the aromatic, or aliphatic functionalization to CNT/graphene, carbonyl functionalization may have less effectiveness for energy transfer. *Y.*

Wang et al.[77] found that the spectrum of functional group butyl have a good overlap with spectrum of graphene and drew a conclusion that butyl functionalization could make prominent reduction of interfacial thermal resistance between graphene and polymer. This study examined the carbonyl functional group on graphene as well. The correlation index between the spectra of graphene and carbonyl was low and this observation concluded that carbonyl was not an effective functional group for interfacial thermal transport between graphene and polymer. In our study, carbonyl functional group seems to be very effective for energy transfer based on the observation of spectra overlap between CNT and crosslinks. It suggests that carbonyl functional group inside crosslinks, bonded to crystalline material such as CNTs can be more effective for energy exchange compared to just attaching functional groups to the crystalline materials.

4.2.3 Spectral Temperature

The spectral temperature change of a frequency band with time explains the energy decay of that band of CNT. In this context, the difference between spectral temperature, T_{sp}, of CNT and the temperature of PEK, i.e, ΔT, is shown in Fig. 29 for 4 different frequency bands. We averaged the spectral temperature data over 10 samples to estimate the spectral temperature decay in time. An exponential function is fitted to this temperature difference in each frequncy band in order to find its relaxation time. All the fitted relaxation times are tabulated in Table 5. In all cases, spectral temperature of the 1st frequency band (0-9THz) decay fastest compared to the other frequncy bands. The fast decay indicates that the low frequency phonons efficiently couple and are dominant for energy transfer at CNT-PEK interface. When the number of crosslinks increases, the relaxation time of 1st band, τ_1, becomes smaller, suggesting a faster energy transfer across the interface. Similar to the 1st frequncy band, energy in 2nd, 3rd and 4th frequency

bands decay faster as number of bonds increases from no crosslinks case to 10 crosslinks case. Thereafter, however, the change in relaxation time is not signficant and decreasing trend is also not consistent. We believe that this could be partly be due to error associated with fitting the data to exponential fit and partly due to the inherent fluctuations in the data obtained from MD simulations. It was observed that the total relaxation time, τ, corresponding to total temperature decay also decreases with increasing number of bonds. This relaxation time is influenced by the CNT interband energy transfer in addition to the interfacial thermal energy transfer [50]. Overall, after observing the relaxation times of different frequency bands, it can be concluded that not only lower frequency phonons but also higher frequency phonons (to some degree) effciently couple across the CNT-PEK interface with increasing number of crosslinks.

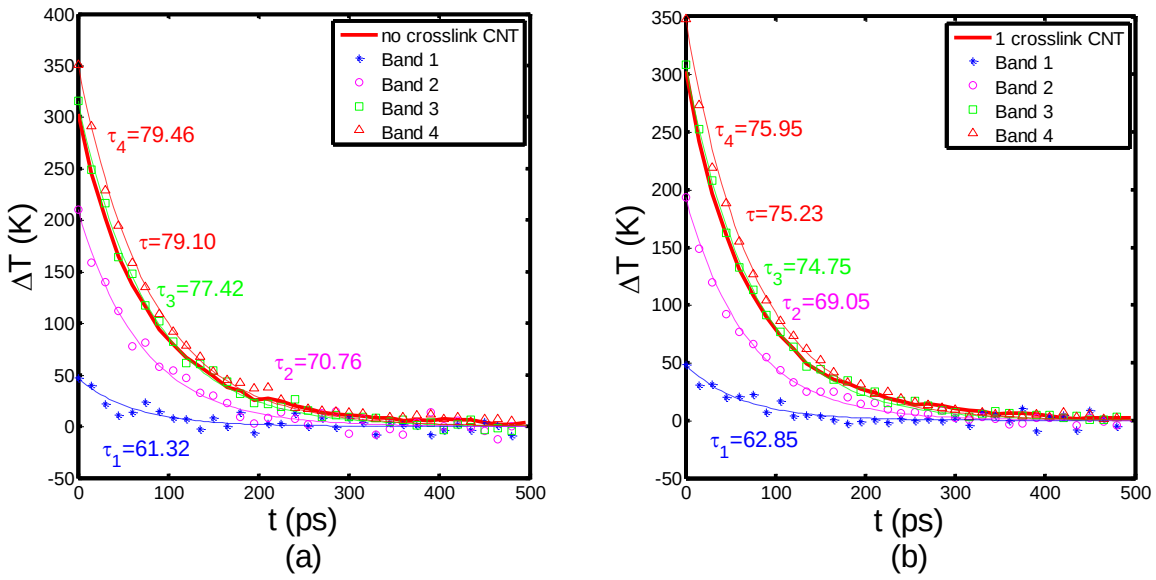

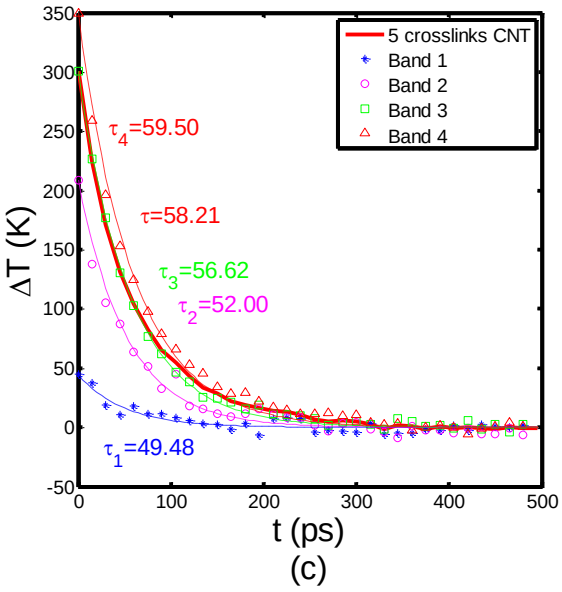
5 crosslinks CNT
Band 1
Band 2
Band 3
Band 4
τ4=59.50
τ=58.21
τ3=56.62
τ2=52.00
τ1=49.48
ΔT (K)
t (ps)

(c)

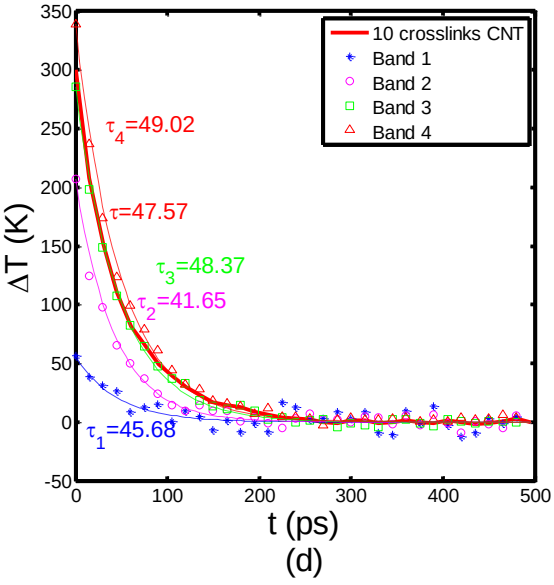
10 crosslinks CNT
Band 1
Band 2
Band 3
Band 4
τ4=49.02
τ=47.57
τ3=48.37
τ2=41.65
τ1=45.68
ΔT (K)
t (ps)

(d)

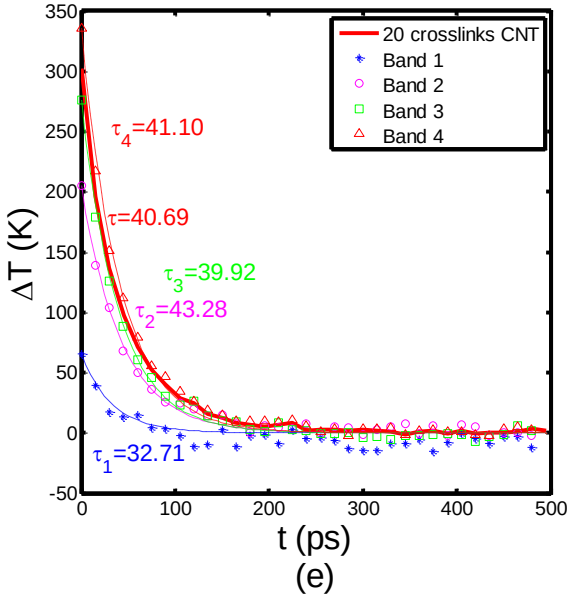
20 crosslinks CNT
Band 1
Band 2
Band 3
Band 4
τ4=41.10
τ=40.69
τ3=39.92
τ2=43.28
τ1=32.71
ΔT (K)
t (ps)

(e)

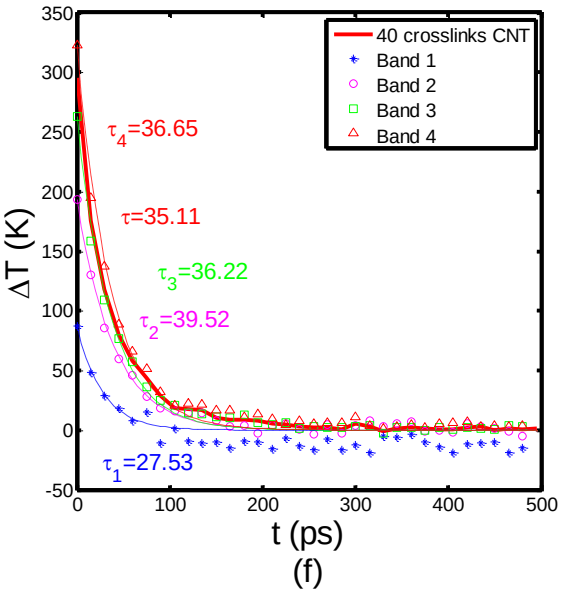
40 crosslinks CNT
Band 1
Band 2
Band 3
Band 4
τ4=36.65
τ=35.11
τ3=36.22
τ2=39.52
τ1=27.53
ΔT (K)
t (ps)

(f)

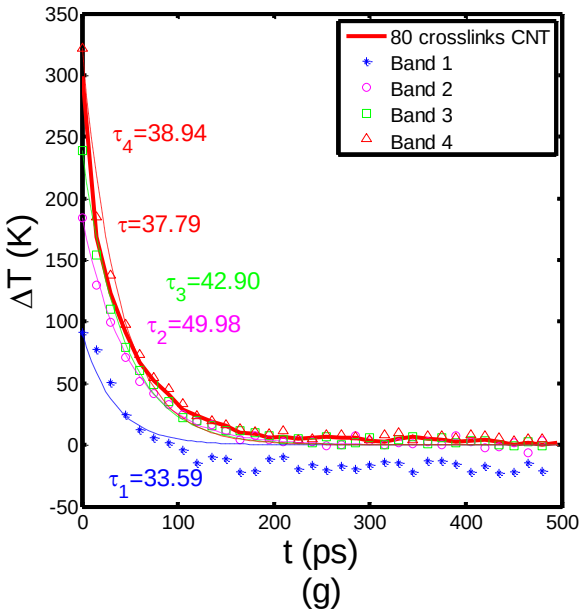

Figure 29: Spectral temperatue decay of different frequency bands for (a) no crosslinks case, (b) 1 crosslink case, (c) 5 crosslinks case, (d) 10 crosslinks case, (e) 20 crosslinks case, (f) 40 crosslinks case, (g) 80 crosslinks case.

Table 5. Relaxation Time of Spectral Temperature in Different Cases

Cases	τ_1 (ps)	τ_2 (ps)	τ_3 (ps)	τ_4 (ps)
No crosslinks	61.32	70.76	77.42	79.46
1 crosslink	62.85	69.05	74.75	75.95
5 crosslinks	49.48	52.00	56.62	59.50
10 crosslinks	45.68	41.65	48.37	49.02
20 crosslinks	32.71	43.28	39.92	41.10
40 crosslinks	27.53	39.52	36.22	36.55
80 crosslinks	33.59	49.98	42.90	38.94

In summary, Chapter 4 presents the TBC calculations at PEK/CNT interfaces and spectral analysis to elucidate energy transfer in frequency domain using spectral energy density (SED) methodology and spectral temperature. The cases studied include no-crosslink, 1 crosslink, 5 crosslinks, 10 crosslinks, 20 crosslinks, 40 crosslinks and 80 crosslinks. The results indicate that increasing number of crosslinks bonded on CNT enhances the TBC and energy transfer between CNT and PEK. Energy transfer in low frequency band (0-9 THz), dominating thermal transport at the interface, is more effective as number of crosslinks increases. Compared with energy transfer at low frequency band, the functionalization also exhibits enhanced energy transfer at mid and high frequency bands, which means functionalization may also assists the optical phonon energies exchange from CNT to PEK. The effect of functionalization on increasing TBC will be saturated after some number of the bonded crosslinks, but this degree of functionalization has not been achieved in the experiments and suggests further room for enhancing TBC and fiber thermal conductivity.

CHAPTER 5

CONCLUSION & PERSPECTIVE

NEMD method and spectral energy/temperature analysis have been employed to investigate the covalent functionalization effects on thermal transport at the interface of CNT and amorphous PEK matrix. The NEMD simulations reveal that the functionalization can increase the TBC significantly because of the efficient thermal coupling at the interface. Compared with the case without any functionalization, the 6.25 % functionalization of CNT atoms enhances the interface thermal boundary conductance (TBC) by an order of magnitude, which supports high increase in thermal conductivity of fibers made by extrusion of PEK grafted CNTs in the experiments. The analysis of spectral temperature of different frequency bands of CNT reveals that relaxation time of all bands decrease with increasing number of covalent bonds. Transient energy spectra of atoms in the crosslinks show oxygen atom of OH group of PEK contribute energy transfer in low frequency band while aromatic carbon C_1, and carbonyl carbon C_4 atoms play a more significant role on high frequency bands energy transfer. The high energy peaks, especially in low frequency bands for both CNT and PEK atoms are smoothened and broadened. As the number of bonded crosslinks increases, the energy exchange of O_1, C_1 and C_4 atoms are observed to be more efficient but start saturating as number of bonds increase from 40 to 80.

Polymeric nanocomposites with carbon based fillers have been studied in the past decade. Most of the theoretical and experimental works focus on electrical, thermal and mechanical property enhancement for composites compared to the polymeric matrix. However, understanding of interface thermal transport between carbon based fillers and polymeric matrices is still limited. Since most of the carbon based fillers are crystalline materials while their surroundings are disordered structure, interactions between the vibrational modes in crystalline

material (normal modes) and the particles (propagons, diffusons and locons) vibrational modes of the disordered material can be complicated, which will strongly change the interface thermal transport phenomena. In the future, the research should continue on the study of interface thermal transport by mode-mode interactions for both crystalline and disordered materials and relative contributions of propagons, diffusons and locons to both thermal conductivity and interfacial heat transfer should be investigated. This will provide insights into engineering the interfaces to obtain high conductivity nano-composites and fibers.

The estimation of thermal conductivity of nano-composites and fibers is quite important to reveal the ultimate limits of achievable conductivity. Effective medium theory can be used to get approximate values of conductivity of nano-composites. It needs the thermal conductivities of filler and surrounding matrices in addition to TBC as inputs. In the future, such approach should be taken to estimate thermal conductivities of different nano-composites/fibers, for no-crosslink and crosslink cases, and to analyze how effective thermal conductivity of nano-composites/fibers will change based on functionalization at CNT/PEK interface.

APPENDIX A

Consistent Valence Force Field (CVFF)

Consistent Valence Force Field (CVFF) consists of bonding energy, pair energy, angle energy, dihedral energy and improper energy. The expression is:

$$E_{tot} = E_{ij}^{pair} + E_{ij}^{bond} + E_{ijk}^{angle} + E_{ijkl}^{dihedral} + E_{ijkl}^{improper} \tag{13}$$

The following sections will introduce each component of CVFF:

i. Energy of Non-bonded Particles, E_{ij}^{pair}

There are two components in E_{ij}^{pair} : one is van der Waals (vdW) interaction and the other is electrostatic interaction between electronic charge. vdW is modeled by Lenard-Jones potential:

$$E_{ij}^{LJ} = 4\varepsilon_{ij}\left[\left(\frac{\sigma_{ij}}{r_{ij}}\right)^{12} - \left(\frac{\sigma_{ij}}{r_{ij}}\right)^{6}\right] \tag{14}$$

where $r_{ij} < r_c$; σ is distance for zero potential between two atoms and ε_{ij} is the depth of potential well. The figure below shows the van der Waals (vdW) interaction between 2 non-bonded atoms.

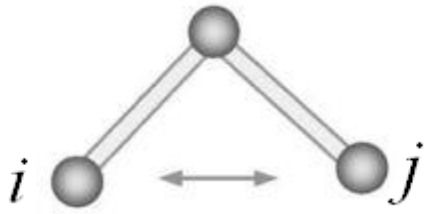

Figure 30: van der Waals (vdW) interaction between 2 non-bonded atoms.

The electrostatic interaction is defined by coulombic law:

$$E_{ij}^{electro} = \frac{q_i q_j}{4\pi\varepsilon_o r_{ij}} \tag{15}$$

where q_i is the charge of particle with unit coulomb (C), and $\varepsilon_o = 8.854188 \text{ x } 10^{-12}$ F/m is permittivity in free space.

ii. Energy of Bonding, E_{ij}^{bond}

The energy of interaction between two bonded atoms is harmonic potential:

$$E_{ij}^{bond} = K_{ij}^{b}(r_{ij} - r_o)^2 \tag{16}$$

where r_o is equilibrium distance between two atoms and K_{ij}^{b} is the stiffness of bonding. The distance between two bonded atoms may be greater and smaller than the equilibrium distance but will not be too far away from the equilibrium position.

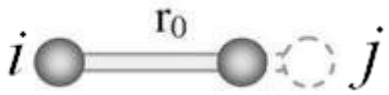

Figure 31: Two bonded atoms in harmonic potential.

iii. Energy of Angle, E_{ijk}^{angle}

The energy of angle also is harmonic potential:

$$E_{ijk}^{angle} = K_{ijk}^{a}(\theta_{ijk} - \theta_o)^2 \tag{17}$$

where θ_o is equilibrium angle between atom *i* and atom *k* while atom *j* is central atom, and K_{ijk}^{a} is the stiffness of angle. The angle picture is shown blow:

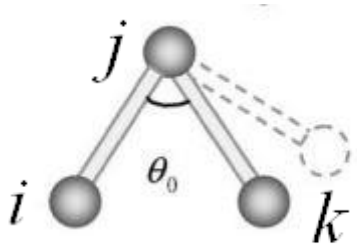

Figure 32: Bonded atoms for the angle term

iv. Energy of Dihedral Angle and Improper Angle, $E_{ijkl}^{dihedral}$ **&** $E_{ijkl}^{improper}$

Both dihedral and improper angles are torsional angles between quadruplets of atoms:

$$E_{ijkl}^{dihedral} = K_{ijkl}^{d}\left[1 + d_d \cos(n_d \phi)\right] \tag{18}$$

$$E_{ijkl}^{improper} = K_{ijkl}^{i}\left[1 + d_i \cos(n_i \phi)\right] \tag{19}$$

where K_{ijkl}^{d} and K_{ijkl}^{i} are the energy barrier height of dihedral angle and improper angle; d_d and d_i (+1 or -1) represent the direction of angle; n_d and n_i are the multiplicities (≥ 0). When the bonding between atom *i* and atom *j* is twisted, the dihedral torsion angle ϕ is formed between plane *ijk* and plane *jkl*.

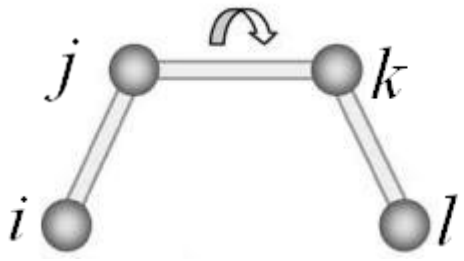

Figure 33: Atoms in dihedral angle potential. The dihedral angle is between plane *jkl* and plane *ijk*.

Similarly, the improper torsion angle ϕ is between plane *ijk* and *jkl*.

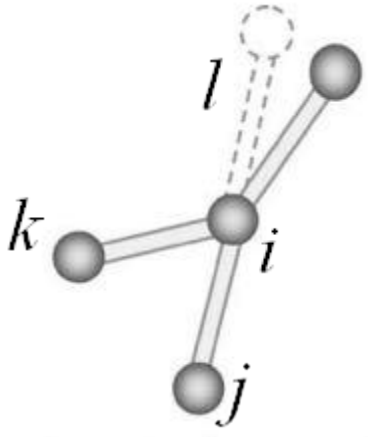

Figure 34: Atoms in improper angle potential. The improper angle is between plane *ijk* and plane *jkl*.

APPENDIX B

Derivation of Spectral Energy Density (SED)

By definition of lattice dynamics [95, 96], the displacement $u(jl,t)$ of *j*-th atom in *l*-th unit cell in crystalline material can be expressed as

$$u(jl,t)=\sum_{k,\nu}U(j,k,\nu)\exp(\mathrm{i}\left[k\cdot r(jl)-\omega(k,\nu)t\right]) \tag{20}$$

where *k* is wave vector, ν is the polarization branch (vibrational mode) for any wave vector and t is time. At this point, $U(j,k,\nu)$ is the vector amplitude giving the information (direction and amplitude) for the motion of *j*-th atom in *l*-th unit cell project to mode (k,ν). After summing over all wave vectors, k, and all polarization branches, ν, the complete displacement, $u(jl,t)$, of specific atom can be defined accurately at each moment, t.

Vector amplitude $U(j,k,\nu)$ multiplied by $\exp(-i\omega(k,\nu)t)$ can be written as:

$$U(j,k,\nu)\cdot\exp(-i\omega(k,\nu)t)=\frac{1}{\left(Nm_j\right)}e\left(j,k,\nu\right)\cdot Q\left(k,\nu,t\right) \tag{21}$$

where N is the number of atoms in every unit cell, m_j is the mass of *j*-th atom and $e\left(j,k,\nu\right)$ is the displacement vector or mode eigenvector. $Q\left(k,\nu,t\right)$ is a complex quantity varying with time and dependent on mode. To ensure the displacement of *j*-th atom is real, $Q\left(-k,\nu,t\right)=Q^{*}\left(k,\nu,t\right)$. By reverse Fourier Transform, the normal mode or normal mode coordinate can be written as:

$$Q\left(k,\nu,t\right)=\sum_{jl}\sqrt{\frac{m_j}{N}}u(jl,t)\exp(-i\cdot k\cdot r(jl))e^{*}\left(j,k,\nu\right) \tag{22}$$

After that, the time-averaged normal mode kinetic energy is summed over all the atoms of all unit cells, which can be written as:

$$\overline{T}(k,\nu)=\frac{1}{\tau_o}\int_0^{\tau_o}\frac{1}{2}\dot{Q}^*(k,\nu,t)\dot{Q}(k,\nu,t)dt \tag{23}$$

As the normal mode kinetic energy is transformed from time domain to frequency domain by Parseval's theorem, the average normal mode kinetic energy can be written as:

$$\overline{T}(k,\nu)=\frac{1}{4\tau_o}\left|\int_0^{\tau_o}\frac{1}{\sqrt{2\pi}}\dot{Q}(k,\nu,t)\exp(-i\omega t)dt\right|^2 \tag{24}$$

Substituting Eqn. 22 into Eqn. 24 will give the spectral energy density (SED):

$$\theta(\omega,k)=\frac{1}{4\pi\tau_o N}\sum_{ij}m_j\left|\int_0^{\tau_o}\dot{u}(jl,t)\exp[i\cdot k\cdot r(jl)-i\omega t]dt\right|^2 \tag{25}$$

Since the unit cells and wave vectors are along CNT length axis, the SED can be simplified in each dimension α as:

$$\theta(\omega,k)=\frac{m}{2}\sum_j^p\sum_\alpha^3\left|\frac{1}{N}\sum_{l=0}^{N-1}\exp(ik_z z)\int\dot{u}_\alpha(jl,t)\exp(-i\omega t)dt\right|^2 \tag{26}$$

The expression above is normalized SED form which will not influence the qualitative analysis of phonon dispersion [85, 86]. Besides that, using Lorentzian Function to fit the frequency peaks of each mode the phonon lifetimes can be estimated [37, 97-100]. However, identifying the frequency peaks around frequency of normal modes and fitting using Lorentzian Functions can be tricky [101].

APPENDIX C

Transient Spectra of Atoms in 40 & 80 Crosslinks

Fig. 35-40b show 3D transient spectra for C_1, C_4 and O_1 atoms of cross-links for 40 and 80 crosslinks cases and compared with the transient spectra of same atoms in same polymer chains for non-bonded case (presented in Fig. 35-40a).

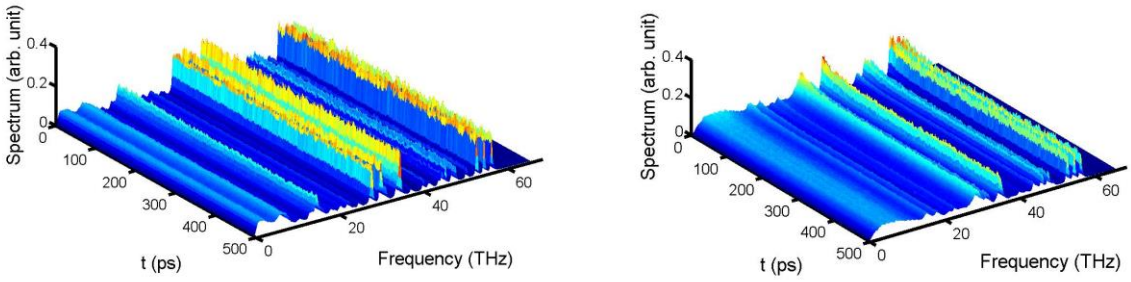

(a) (b)

Figure 35: The transient spectra of aromatic carbon atoms (C_1) in same polymer chains of (a) non-bonded and (b) 40 crosslinks case

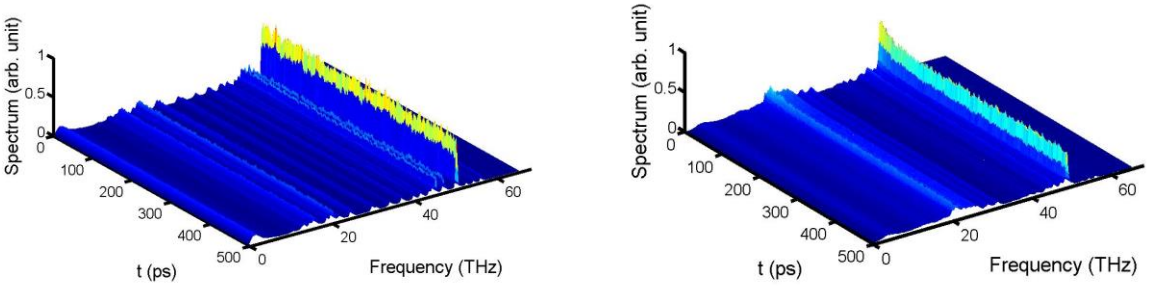

(a) (b)

Figure 36: The transient spectra of carboxyl carbon atoms (C_4) in same polymer chains of (a) non-bonded and (b) 40 crosslinks case.

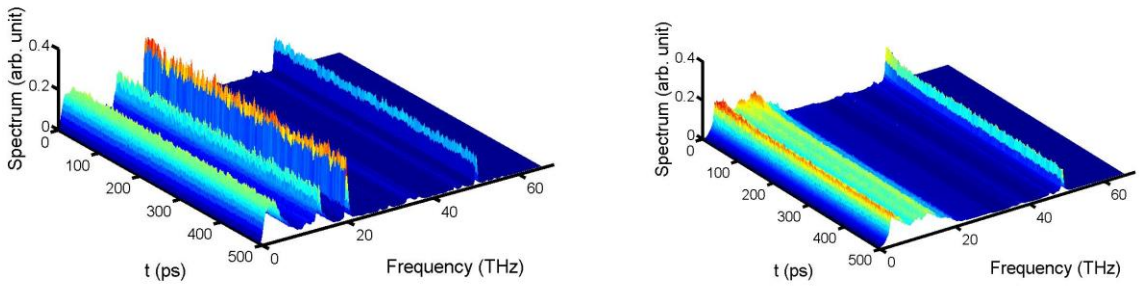

(a) (b)

Figure 37: The transient spectra of carboxyl oxygen atoms (O_1) in same polymer chains of (a) non-bonded and (b) 40 crosslinks case.

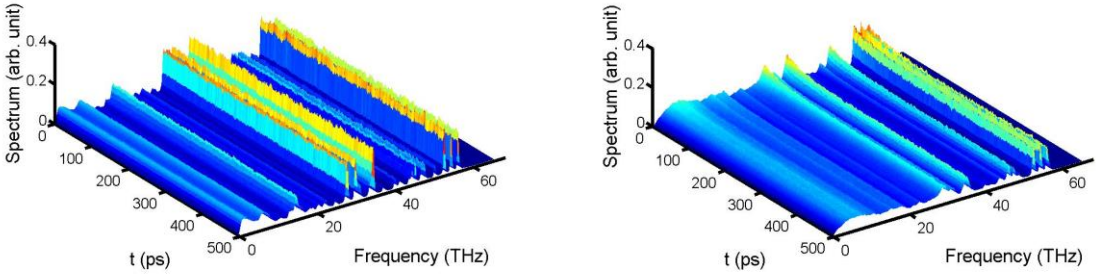

(a) (b)

Figure 38: The transient spectra of aromatic carbon atoms (C_1) in same polymer chains of (a) non-bonded and (b) 80 crosslinks case.

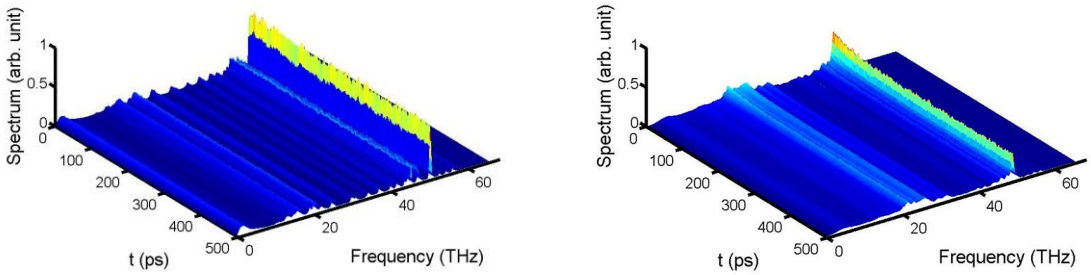

(a) (b)

Figure 39: The transient spectra of carboxyl carbon atoms (C_4) in same polymer chains of (a) non-bonded and (b) 80 crosslinks case.

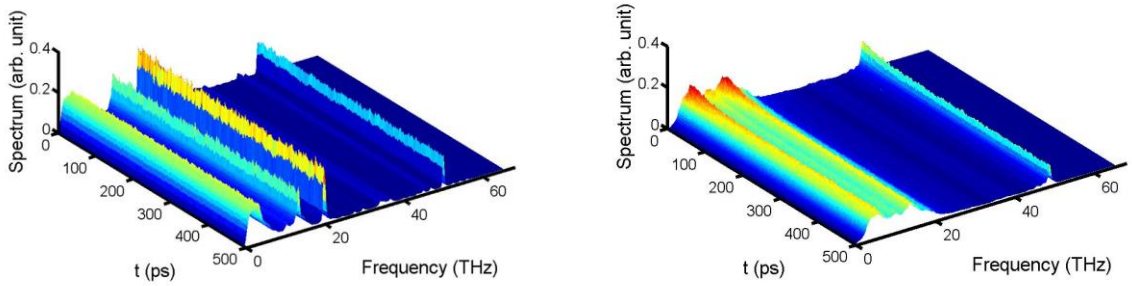

(a) (b)

Figure 40: The transient spectra of carboxyl oxygen atoms (O_1) in same polymer chains of (a) non-bonded and (b) 80 crosslinks case.

REFERENCES

1. Cahill, D.G., et al., *Nanoscale thermal transport. II. 2003-2012.* Applied Physics Reviews, 2014. **1**(1).
2. Han, Z.D. and A. Fina, *Thermal conductivity of carbon nanotubes and their polymer nanocomposites: A review.* Progress in Polymer Science, 2011. **36**(7): p. 914-944.
3. Zweben, C., *Advances in composite materials for thermal management in electronic packaging.* Jom-Journal of the Minerals Metals & Materials Society, 1998. **50**(6): p. 47-51.
4. Diez-Pascual, A.M., et al., *High performance PEEK/carbon nanotube composites compatibilized with polysulfones-II. Mechanical and electrical properties.* Carbon, 2010. **48**(12): p. 3500-3511.
5. Nika, D.L. and A.A. Balandin, *Two-dimensional phonon transport in graphene.* Journal of Physics-Condensed Matter, 2012. **24**(23).
6. Thostenson, E.T., Z.F. Ren, and T.W. Chou, *Advances in the science and technology of carbon nanotubes and their composites: a review.* Composites Science and Technology, 2001. **61**(13): p. 1899-1912.
7. Boudenne, A., et al., *Electrical and thermal behavior of polypropylene filled with copper particles.* Composites Part a-Applied Science and Manufacturing, 2005. **36**(11): p. 1545-1554.
8. Zhou, W.Y., et al., *Thermal conductivity of boron nitride reinforced polyethylene composites.* Materials Research Bulletin, 2007. **42**(10): p. 1863-1873.
9. Yu, S.Z., P. Hing, and X. Hu, *Thermal conductivity of polystyrene-aluminum nitride composite.* Composites Part a-Applied Science and Manufacturing, 2002. **33**(2): p. 289-292.
10. Guthy, C., et al., *Thermal conductivity of single-walled carbon nanotube/PMMA nanocomposites.* Journal of Heat Transfer-Transactions of the Asme, 2007. **129**(8): p. 1096-1099.
11. Huxtable, S.T., et al., *Interfacial heat flow in carbon nanotube suspensions.* Nature Materials, 2003. **2**(11): p. 731-734.
12. Shenogin, S., et al., *Role of thermal boundary resistance on the heat flow in carbon-nanotube composites.* Journal of Applied Physics, 2004. **95**(12): p. 8136-8144.
13. Moon, J., et al., *Note: Thermal conductivity measurement of individual poly(ether ketone)/carbon nanotube fibers using a steady-state dc thermal bridge method.* Review of Scientific Instruments, 2012. **83**(1).
14. Hsieh, W.P., et al., *Testing the minimum thermal conductivity model for amorphous polymers using high pressure.* Physical Review B, 2011. **83**(17).
15. Terao, T., E. Lussetti, and F. Muller-Plathe, *Nonequilibrium molecular dynamics methods for computing the thermal conductivity: Application to amorphous polymers.* Physical Review E, 2007. **75**(5).
16. Pal, S., G. Balasubramanian, and I.K. Puri, *Reducing thermal transport in electrically conducting polymers: Effects of ordered mixing of polymer chains.* Applied Physics Letters, 2013. **102**(2).
17. Zhao, J.H., et al., *Thermal conductivity dependence on chain length in amorphous polymers.* Journal of Applied Physics, 2013. **113**(18).
18. Liu, J., M. Alhashme, and R.G. Yang, *Thermal Transport across Carbon Nanotube Connected by Molecular Linkers.* Proceedings of the Asme International Mechanical Engineering Congress and Exposition, 2011, Vol 10, Pts a and B, 2012: p. 395-396.
19. Liu, J. and R.G. Yang, *Length-dependent thermal conductivity of single extended polymer chains.* Physical Review B, 2012. **86**(10).
20. E. Fermi, J.P.a.S.U., *Los Alamos Report No. LA 1940*. 1955.
21. Henry, A. and G. Chen, *High Thermal Conductivity of Single Polyethylene Chains Using Molecular Dynamics Simulations.* Physical Review Letters, 2008. **101**(23): p. -.

22. Henry, A. and G. Chen, *Anomalous heat conduction in polyethylene chains: Theory and molecular dynamics simulations.* Physical Review B, 2009. **79**(14).
23. McGaughey, A.J.H. and M. Kaviany, *Quantitative validation of the Boltzmann transport equation phonon thermal conductivity model under the single-mode relaxation time approximation.* Physical Review B, 2004. **69**(9): p. -.
24. McGaughey, A.J.H. and M. Kaviany, *Thermal conductivity decomposition and analysis using molecular dynamics simulations. Part I. Lennard-Jones argon.* International Journal of Heat and Mass Transfer, 2004. **47**(8-9): p. 1783-1798.
25. Chen, G., *Nanoscale energy transport and conversion : a parallel treatment of electrons, molecules, phonons, and photons*. MIT-Pappalardo series in mechanical engineering. 2005, Oxford ; New York: Oxford University Press. xxiii, 531 p.
26. Fedorov, V.I. and V.I. Machuev, *Thermal Conductivity of Pbte,Snte, and Gete in Solid and Liquid Phases.* Soviet Physics Solid State,Ussr, 1969. **11**(5): p. 1116-&.
27. Robbins, A.B. and A.J. Minnich, *Crystalline polymers with exceptionally low thermal conductivity studied using molecular dynamics.* Applied Physics Letters, 2015. **107**(20).
28. Allen, P.B., et al., *Diffusons, locons and propagons: character of atomic vibrations in amorphous Si.* Philosophical Magazine B-Physics of Condensed Matter Statistical Mechanics Electronic Optical and Magnetic Properties, 1999. **79**(11-12): p. 1715-1731.
29. Liu, X., et al., *Low temperature study of loss mechanisms of mechanical oscillators.* Physica B, 2002. **316**: p. 393-396.
30. Lv, W. and A. Henry, *Direct calculation of modal contributions to thermal conductivity via Green-Kubo modal analysis.* New Journal of Physics, 2016. **18**.
31. Larkin, J.M. and A.J.H. McGaughey, *Predicting alloy vibrational mode properties using lattice dynamics calculations, molecular dynamics simulations, and the virtual crystal approximation.* Journal of Applied Physics, 2013. **114**(2).
32. Larkin, J.M. and A.J.H. McGaughey, *Thermal conductivity accumulation in amorphous silica and amorphous silicon.* Physical Review B, 2014. **89**(14).
33. Jain, R., et al., *Processing, structure and properties of poly(ether ketone) grafted few wall carbon nanotube composite fibers.* Polymer, 2010. **51**(17): p. 3940-3947.
34. Salaway, R.N. and L.V. Zhigilei, *Molecular dynamics simulations of thermal conductivity of carbon nanotubes: Resolving the effects of computational parameters.* International Journal of Heat and Mass Transfer, 2014. **70**: p. 954-964.
35. Balandin, A.A., et al., *Superior thermal conductivity of single-layer graphene.* Nano Letters, 2008. **8**(3): p. 902-907.
36. Ghosh, S., et al., *Extremely high thermal conductivity of graphene: Prospects for thermal management applications in nanoelectronic circuits.* Applied Physics Letters, 2008. **92**(15): p. -.
37. Feng, T.L., et al., *Spectral phonon mean free path and thermal conductivity accumulation in defected graphene: The effects of defect type and concentration.* Physical Review B, 2015. **91**(22).
38. Hu, L.B., D.S. Hecht, and G. Gruner, *Carbon Nanotube Thin Films: Fabrication, Properties, and Applications.* Chemical Reviews, 2010. **110**(10): p. 5790-5844.
39. Wang, Y., S.Y. Chen, and X.L. Ruan, *Tunable thermal rectification in graphene nanoribbons through defect engineering: A molecular dynamics study.* Applied Physics Letters, 2012. **100**(16).
40. Luo, T.F. and J.R. Lloyd, *Non-equilibrium molecular dynamics study of thermal energy transport in Au-SAM-Au junctions.* International Journal of Heat and Mass Transfer, 2010. **53**(1-3): p. 1-11.
41. Gulotty, R., et al., *Effects of Functionalization on Thermal Properties of Single-Wall and Multi-Wall Carbon Nanotube-Polymer Nanocomposites.* Acs Nano, 2013. **7**(6): p. 5114-5121.
42. Kumlutas, D., I.H. Tavman, and M.T. Coban, *Thermal conductivity of particle filled polyethylene composite materials.* Composites Science and Technology, 2003. **63**(1): p. 113-117.

43. Mamunya, Y.P., et al., *Electrical and thermal conductivity of polymers filled with metal powders.* European Polymer Journal, 2002. **38**(9): p. 1887-1897.
44. Ohashi, M., et al., *Spherical aluminum nitride fillers for heat-conducting plastic packages.* Journal of the American Ceramic Society, 2005. **88**(9): p. 2615-2618.
45. Gu, J.W., et al., *Thermal Conductivity and Mechanical Properties of Aluminum Nitride Filled Linear Low-Density Polyethylene Composites.* Polymer Engineering and Science, 2009. **49**(5): p. 1030-1034.
46. Zhou, W.Y., et al., *Thermally conductive silicone rubber reinforced with boron nitride particle.* Polymer Composites, 2007. **28**(1): p. 23-28.
47. Varshney, V., et al., *Effect of Curing and Functionalization on the Interface Thermal Conductance in Carbon Nanotube-Epoxy Composites.* Jom, 2013. **65**(2): p. 140-146.
48. Kuang, Y.D. and B.L. Huang, *Effects of covalent functionalization on the thermal transport in carbon nanotube/polymer composites: A multi-scale investigation.* Polymer, 2015. **56**: p. 563-571.
49. Hida, S., et al., *Thermal resistance and phonon scattering at the interface between carbon nanotube and amorphous polyethylene.* International Journal of Heat and Mass Transfer, 2013. **67**: p. 1024-1029.
50. Carlborg, C.F., J. Shiomi, and S. Maruyama, *Thermal boundary resistance between single-walled carbon nanotubes and surrounding matrices.* Physical Review B, 2008. **78**(20): p. -.
51. Babaei, H., P. Keblinski, and J.M. Khodadadi, *Thermal conductivity enhancement of paraffins by increasing the alignment of molecules through adding CNT/graphene.* International Journal of Heat and Mass Transfer, 2013. **58**(1-2): p. 209-216.
52. Shiomi, J., *NONEQUILIRIUM MOLECULAR DYNAMICS METHODS FOR LATTICE HEAT CONDUCTION CALCULATIONS*. Vol. 17. 2014: Begell House. Inc. Publishers.
53. Varshney, V., et al., *Modeling of Thermal Conductance at Transverse CNT-CNT Interfaces.* Journal of Physical Chemistry C, 2010. **114**(39): p. 16223-16228.
54. Roy, A.K., et al., *Importance of Interfaces in Governing Thermal Transport in Composite Materials: Modeling and Experimental Perspectives.* Acs Applied Materials & Interfaces, 2012. **4**(2): p. 545-563.
55. Lukes, J.R. and H.L. Zhong, *Thermal conductivity of individual single-wall carbon nanotubes.* Journal of Heat Transfer-Transactions of the Asme, 2007. **129**(6): p. 705-716.
56. Savin, A.V., B.B. Hu, and Y.S. Kivshar, *Thermal conductivity of single-walled carbon nanotubes.* Physical Review B, 2009. **80**(19).
57. Bi, K.D., et al., *Molecular dynamics simulation of thermal conductivity of single-wall carbon nanotubes.* Physics Letters A, 2006. **350**(1-2): p. 150-153.
58. Shelly, R.A., K. Toprak, and Y. Bayazitoglu, *Nose-Hoover thermostat length effect on thermal conductivity of single wall carbon nanotubes.* International Journal of Heat and Mass Transfer, 2010. **53**(25-26): p. 5884-5887.
59. Berber, S., Y.K. Kwon, and D. Tomanek, *Unusually high thermal conductivity of carbon nanotubes.* Physical Review Letters, 2000. **84**(20): p. 4613-4616.
60. Cao, A.J. and J.M. Qu, *Size dependent thermal conductivity of single-walled carbon nanotubes.* Journal of Applied Physics, 2012. **112**(1).
61. Ren, C.L., et al., *Thermal Conductivity of Single-Walled Carbon Nanotubes under Axial Stress.* Journal of Physical Chemistry C, 2010. **114**(13): p. 5786-5791.
62. Che, J.W., T. Cagin, and W.A. Goddard, *Thermal conductivity of carbon nanotubes.* Nanotechnology, 2000. **11**(2): p. 65-69.
63. Ong, Z.Y. and E. Pop, *Effect of substrate modes on thermal transport in supported graphene.* Physical Review B, 2011. **84**(7).

64. Ong, Z.Y. and E. Pop, *Frequency and polarization dependence of thermal coupling between carbon nanotubes and SiO2.* Journal of Applied Physics, 2010. **108**(10).
65. Ong, Z.Y. and E. Pop, *Molecular dynamics simulation of thermal boundary conductance between carbon nanotubes and SiO2.* Physical Review B, 2010. **81**(15).
66. Ong, Z.Y., E. Pop, and J. Shiomi, *Reduction of phonon lifetimes and thermal conductivity of a carbon nanotube on amorphous silica.* Physical Review B, 2011. **84**(16).
67. Luo, T.F. and J.R. Lloyd, *Enhancement of Thermal Energy Transport Across Graphene/Graphite and Polymer Interfaces: A Molecular Dynamics Study.* Advanced Functional Materials, 2012. **22**(12): p. 2495-2502.
68. Varshney, V., et al., *A molecular dynamics study of epoxy-based networks: Cross-linking procedure and prediction of molecular and material properties.* Macromolecules, 2008. **41**(18): p. 6837-6842.
69. Clancy, T.C. and T.S. Gates, *Modeling of interfacial modification effects on thermal conductivity of carbon nanotube composites.* Polymer, 2006. **47**(16): p. 5990-5996.
70. Li, Y. and G.D. Seidel, *Multiscale modeling of the effects of nanoscale load transfer on the effective elastic properties of unfunctionalized carbon nanotube-polyethylene nanocomposites.* Modelling and Simulation in Materials Science and Engineering, 2014. **22**(2).
71. Kim, G.H., et al., *High thermal conductivity in amorphous polymer blends by engineered interchain interactions.* Nature Materials, 2015. **14**(3): p. 295-300.
72. Singh, V., et al., *High thermal conductivity of chain-oriented amorphous polythiophene.* Nature Nanotechnology, 2014. **9**(5): p. 384-390.
73. Losego, M.D., et al., *Effects of chemical bonding on heat transport across interfaces.* Nature Materials, 2012. **11**(6): p. 502-506.
74. Choi, J.Y., et al., *In-situ grafting of hyperbranched poly(ether ketone)s onto multiwalled carbon nanotubes via the A(3)+B-2 approach.* Macromolecules, 2007. **40**(13): p. 4474-4480.
75. Choi, J.Y., et al., *In situ grafting of carboxylic acid-terminated hyperbranched poly (ether-ketone) to the surface of carbon nanotubes.* Polymer, 2007. **48**(14): p. 4034-4040.
76. Liu, X.J., G. Zhang, and Y.W. Zhang, *Thermal Conduction Across Graphene Cross-Linkers.* Journal of Physical Chemistry C, 2014. **118**(23): p. 12541-12547.
77. Wang, Y., et al., *Effect of Covalent Functionalization on Thermal Transport across Graphene-Polymer Interfaces.* Journal of Physical Chemistry C, 2015. **119**(22): p. 12731-12738.
78. Wang, M.C., et al., *Enhanced interfacial thermal transport across graphene-polymer interfaces by grafting polymer chains.* Carbon, 2015. **85**: p. 414-421.
79. Luo, T.F. and J.R. Lloyd, *Equilibrium Molecular Dynamics Study of Lattice Thermal Conductivity/Conductance of Au-SAM-Au Junctions.* Journal of Heat Transfer-Transactions of the Asme, 2010. **132**(3).
80. Hagler, A.T. and S. Lifson, *Energy Functions for Peptides and Proteins .2. Amide Hydrogen-Bond and Calculation of Amide Crystal Properties.* Journal of the American Chemical Society, 1974. **96**(17): p. 5327-5335.
81. Chen, X. and G.X. Cao, *A structural mechanics study of single-walled carbon nanotubes generalized from atomistic simulation.* Nanotechnology, 2006. **17**(4): p. 1004-1015.
82. Mayo, S.L., B.D. Olafson, and W.A. Goddard, *Dreiding - a Generic Force-Field for Molecular Simulations.* Journal of Physical Chemistry, 1990. **94**(26): p. 8897-8909.
83. Zang, J.L., et al., *A comparative study of Young's modulus of single-walled carbon nanotube by CPMD, MD and first principle simulations.* Computational Materials Science, 2009. **46**(3): p. 621-625.

84. Xiao, J.R., B.A. Gama, and J.W. Gillespie, *An analytical molecular structural mechanics model for the mechanical properties of carbon nanotubes.* International Journal of Solids and Structures, 2005. **42**(11-12): p. 3075-3092.
85. Chen, L. and S. Kumar, *Heat Dissipation Mechanism at Carbon Nanotube Junctions on Silicon Oxide Substrate.* Journal of Heat Transfer-Transactions of the Asme, 2014. **136**(5).
86. Thomas, J.A., et al., *Predicting phonon dispersion relations and lifetimes from the spectral energy density.* Physical Review B, 2010. **81**(8).
87. Varshney, V., A.K. Roy, and J.W. Baur, *Modeling the Role of Bulk and Surface Characteristics of Carbon Fiber on Thermal Conductance across the Carbon-Fiber/Matrix Interface.* Acs Applied Materials & Interfaces, 2015. **7**(48): p. 26674-26683.
88. Varshney, V., et al., *Modeling of Thermal Transport in Pillared-Graphene Architectures.* Acs Nano, 2010. **4**(2): p. 1153-1161.
89. Roy, A.K., et al., *Thermal interface tailoring in composite materials.* Diamond and Related Materials, 2010. **19**(2-3): p. 268-272.
90. Shi, J.J., et al., *Thermal transport across carbon nanotube-graphene covalent and van der Waals junctions.* Journal of Applied Physics, 2015. **118**(4).
91. Maruyama, S., et al., *Anisotropic Heat Transfer of Single-Walled Carbon Nanotubes.* Journal of Thermal Science and Technology, 2006. **1**(2): p. 138-148.
92. Rajabpour, A. and S. Volz, *Thermal boundary resistance from mode energy relaxation times: Case study of argon-like crystals by molecular dynamics.* Journal of Applied Physics, 2010. **108**(9).
93. Bryning, M.B., et al., *Thermal conductivity and interfacial resistance in single-wall carbon nanotube epoxy composites.* Applied Physics Letters, 2005. **87**(16).
94. Nan, C.W., et al., *Interface effect on thermal conductivity of carbon nanotube composites.* Applied Physics Letters, 2004. **85**(16): p. 3549-3551.
95. Kittel, C., *Introduction to solid state physics*. 8th ed. 2005, Hoboken, NJ: Wiley. xix, 680 p.
96. Dove, M.T., *Introduction to Lattice Dynamics*. Cambridge Topics in Mineral Physics and Chemistry, ed. R.C.L. Andrew Putnis. 1993: Cambridge University Press. 258.
97. Qiu, B. and X.L. Ruan, *Spectra phonon mean free path and thermal conductivity of suspended and supported graphene.* Nano Letters, 2011: p. submitted.
98. Feng, T.L., B. Qiu, and X.L. Ruan, *Anharmonicity and necessity of phonon eigenvectors in the phonon normal mode analysis.* Journal of Applied Physics, 2015. **117**(19).
99. Chen, L. and S. Kumar, *Thermal transport in graphene supported on copper.* Journal of Applied Physics, 2012. **112**(4).
100. Feng, T.L. and X.L. Ruan, *Prediction of Spectral Phonon Mean Free Path and Thermal Conductivity with Applications to Thermoelectrics and Thermal Management: A Review.* Journal of Nanomaterials, 2014.
101. Larkin, J.M., et al., *Comparison and Evaluation of Spectral Energy Methods for Predicting Phonon Properties.* Journal of Computational and Theoretical Nanoscience, 2014. **11**(1): p. 249-256.